

# Two-dimensional coherent spectroscopy of disordered superconductors in the narrow-band and broad-band limits

Naoto Tsuji<sup>1,2</sup>

<sup>1</sup>*Department of Physics, University of Tokyo, Hongo, Tokyo 113-0033, Japan*

<sup>2</sup>*RIKEN Center for Emergent Matter Science (CEMS), Wako 351-0198, Japan*

(Dated: September 5, 2025)

We theoretically analyze two-dimensional coherent spectroscopy (2DCS) signals for disordered superconductors in two limits: One is the narrow-band limit with sinusoidal pulse waves, and the other is the broad-band limit with delta-function pulses. While the 2DCS signal in the narrow-band limit is related to the third-order nonlinear susceptibilities  $\chi^{(3)}(3\Omega; \Omega, \Omega, \Omega)$  (third harmonic generation) and  $\chi^{(3)}(\Omega; \Omega, \Omega, -\Omega)$  (ac Kerr effect), we find that in the broad-band limit the signal along the diagonal and horizontal lines in the two-dimensional frequency space is related to another nonlinear susceptibility  $\chi^{(3)}(\Omega; \Omega, 0, 0)$  (dc Kerr effect). We numerically evaluate those susceptibilities for a lattice model of superconductors based on the BCS mean-field theory and self-consistent Born approximation for impurities. The 2DCS signals in the narrow-band and broad-band limits show threshold and resonance behaviors at the superconducting-gap frequency, respectively, whose physical origin is discussed in light of quasiparticle and Higgs-mode excitations.

## I. INTRODUCTION

Two-dimensional coherent spectroscopy (2DCS) [1–7] is recently adopted as a tool to probe nonlinear optical response of various quantum materials using multiple laser pulses. By controlling delay times between pulses, one can map out the signal in a multi-dimensional frequency space, which brings fruitful information that is hard to access with other spectroscopy techniques such as absorption and reflection spectroscopies. In particular, one can subtract linear response components systematically by taking the difference between different pulse configurations, which allows one to extract nonlinear response components accurately even at the first harmonic frequency of injected pulses.

The 2DCS is useful in detecting collective modes in a condensed phase of materials including quantum magnets and superconductors [8]. The presence of those collective modes tells us key aspects of quantum phases, e.g., symmetries, fluctuations, phase transitions, hidden orders, and so on. In superconductors, there exists the Higgs mode [9–12], i.e., an amplitude mode of the superconducting order parameter, which does not linearly couple to electromagnetic fields in usual situations (an exception is the case where Cooper pairs have nonzero center-of-mass momentum [13–18]). Previously, the Higgs mode has been observed by a nonlinear response setup such as Raman scattering [19–25], pump-probe spectroscopy [26–29], and third harmonic generation [27, 30, 31] (see also Refs. [32–37]). On the other hand, it is not straightforward to extract the contribution of the Higgs mode separately, as individual excitations of quasiparticles also contribute to the signal at similar frequencies (which correspond to the superconducting gap size). This raises a question of finding other measurement protocols that can detect the effect of collective modes selectively.

Recently, the 2DCS has been applied to study nonlinear response of NbN and MgB<sub>2</sub> superconductors in

the terahertz regime [38, 39]. For NbN, the temperature dependence of the first harmonic contribution of the 2DCS signal with a narrow-band pulse shows a peak when the frequency agrees with the superconducting gap ( $\Omega = 2\Delta$ ). In contrast, the 2DCS for MgB<sub>2</sub> superconductors does not show such a peak but exhibits monotonic temperature dependence. The interpretation of the results has been discussed in connection to collective modes of superconductors. The 2DCS has also been employed to study nickelate superconductors [40] and cuprates [41]. Theoretically, the 2DCS has been analyzed for multiband superconductors [42], layered superconductors [43], correlated insulators [44], and antiferromagnets [45].

Motivated by the recent experiments, in this paper we study the 2DCS for disordered superconductors in two limits: One is the narrow-band limit where pulses are modeled as sinusoidal waves, and the other is the broad-band limit where pulses are treated as delta functions. While the first harmonic component of the 2DCS signal is described by the ac Kerr susceptibility  $\chi^{(3)}(\Omega; \Omega, \Omega, -\Omega)$ , we find that the 2DCS signal in the broad-band limit is related to the dc Kerr susceptibility  $\chi^{(3)}(\Omega; \Omega, 0, 0)$ . We also derive a general formula for the 2DCS with general pulse wave forms, which is given by the frequency integral of the third-order nonlinear susceptibility with different frequency combinations. We numerically evaluate the ac and dc Kerr susceptibilities for a lattice model of disordered superconductors.

As suggested for the optical conductivity [46] and third harmonic generation [47–51], disorders play a pivotal role in understanding (non)linear response of superconductors (phonon retardation effects also play a role [52]). In fact, the Higgs mode has been shown to contribute dominantly to the THG resonance at half of the gap frequency ( $\Omega = \Delta$ ) in the dirty regime, while the Higgs mode becomes less dominant than quasiparticles in the clean regime [53]. To treat disorders in the dirty regime, the system has to satisfy the following length scale sepa-

ration:

$$\frac{v_F}{W} \ll \frac{v_F}{\gamma} \ll \frac{v_F}{2\Delta} \ll L. \quad (1)$$

Here  $v_F$  is the Fermi velocity,  $W$  is the bandwidth of electrons,  $\gamma$  is the disorder scattering rate,  $2\Delta$  is the superconducting gap, and  $L$  is the linear system size. Note that we set  $\hbar = 1$  throughout this paper. In the dirty regime, the coherence length  $\frac{v_F}{2\Delta}$  must be longer than the mean free path  $\frac{v_F}{\gamma}$ . To avoid finite-size effects, the linear system size should be taken to be much longer than the coherence length. When  $\gamma$  becomes comparable to  $W$ , the effect of localization begins to emerge, which is far from experimental situations. Typically, one has  $L \sim 10^{-2}$  [m],  $v_F \sim 10^6$  [m/s],  $2\Delta \sim 10^{12}$  [s $^{-1}$ ],  $\frac{v_F}{2\Delta} \sim 10^{-6}$  [m],  $\frac{v_F}{\gamma} \sim 10^{-8}$ - $10^{-7}$  [m], and  $\frac{v_F}{W} \sim 10^{-9}$  [m] for dirty superconductors in experiments, satisfying the relation (1).

The previous analysis on the 2DCS for disordered superconductors has focused on the narrow-band limit of pulses, and has been based on the simulation of the mean field theory with random disorders in real space [38]. While the effect of disorders is treated exactly in this approach, it is not easy to satisfy the clear scale separation (1), for which one typically requires  $L \gtrsim 100a$  in a lattice model ( $a$  is the lattice constant) [54]. In two dimensions, for instance, the number of lattice sites reaches  $100 \times 100$ , which is computationally demanding. Furthermore, the finite-size scaling is sometimes challenging: For example, there appears a logarithmic correction in the system size dependence of conductance in two dimensions [55–57].

To circumvent those problems, we employ the self-consistent Born approximation [50, 58], which is a semi-classical treatment of disorders that allows one to approach the desired scale separation (1). In fact, we can take  $100 \times 100$  lattice sites within reasonable numerical cost. Since the self-consistent Born approximation is a kind of the mean-field theory for disorders, the results do not significantly depend on the spatial dimension of the system (describing the behavior in large dimensions), and the system size dependence can be numerically well controlled.

Using the self-consistent Born approximation for disorders and BCS approximation for the pairing interaction, we obtain the ac and dc Kerr susceptibilities for disordered superconductors. The results show that the ac Kerr susceptibility shows threshold behavior, i.e., the intensity starts to grow above the superconducting gap frequency ( $\Omega \geq 2\Delta$ ), in both the clean and dirty regimes. Physically, this behavior is mainly mediated by the zero-frequency Higgs mode which is far off-resonant. On the other hand, the dc Kerr susceptibility exhibits a resonance peak at the gap frequency ( $\Omega = 2\Delta$ ), which is mostly mediated by the Higgs mode carrying the frequency  $\Omega$  in the dirty regime. We examine the temperature and disorder dependence of the ac and dc Kerr susceptibilities, and discuss the relation to the experiments.

The paper is organized as follows. In Sec. II, we review the formalism of the linear optical response in the

narrow-band and broad-band limits as a warm up. In Sec. III, we formulate the 2DCS with general pulse wave forms, and derive a formula that relates the 2DCS with the nonlinear susceptibilities. In Sec. IV and Sec. V, we treat the narrow-band and broad-band limits of the 2DCS, respectively. In Sec. VI, we demonstrate the numerical results on the ac and dc Kerr susceptibilities for a lattice model of disordered superconductors. The paper is summarized in Sec. VII with the outlook of future directions of the study.

## II. LINEAR OPTICAL RESPONSE IN THE NARROW-BAND AND BROAD-BAND LIMITS

In this section, we overview the derivation of the linear optical response functions in the narrow-band and broad-band limits, which can be extended to nonlinear responses including the 2DCS in later sections. It has been known that the two limits are intimately related to each other, and both of them can be described by the same response function.

In the narrow-band limit, an injected pulse is a monochromatic wave defined by a vector potential

$$\mathbf{A}(t) = \mathbf{A}e^{-i\Omega t} \quad (2)$$

with a constant amplitude vector  $\mathbf{A}$ . The measured current expanded up to the first order in the drive field is written as

$$\mathbf{j}(t) = \sigma(\Omega)\mathbf{E}(t), \quad (3)$$

where  $\sigma(\Omega)$  is the optical conductivity (i.e., the linear response coefficient), and  $\mathbf{E}(t) = -\partial_t \mathbf{A}(t)$  is the driving electric field. Throughout the paper, we assume that applied pulse fields and induced currents are polarized along the same direction for simplicity, and suppress the vector notation below (for example,  $j(t)$  should be understood as  $\mathbf{e} \cdot \mathbf{j}(t)$  where  $\mathbf{e}$  is the polarization unit vector).

According to the standard linear response theory, the optical conductivity is given by

$$\sigma(\Omega) = \frac{1}{i\Omega} \chi^{(1)}(\Omega), \quad (4)$$

where  $\chi^{(1)}(\Omega)$  is formally defined as

$$\chi^{(1)}(\Omega) = \int_{-\infty}^{\infty} d\bar{t} e^{i\Omega(t-\bar{t})} \left. \frac{\delta j(t)}{\delta A(\bar{t})} \right|_{A=0}. \quad (5)$$

Note that the right hand side of Eq. (5) does not depend on  $t$  due to the time-translation symmetry. The current is directly written in terms of  $\chi^{(1)}$  as

$$j(t) = \chi^{(1)}(\Omega)A(t) \quad (6)$$

up to the first order in  $A$ .

In the broad-band limit, the driving field is modeled with a delta-function pulse,

$$E(t) = A\delta(t). \quad (7)$$

Here  $A$  is the amplitude of the pulse having the dimension of the vector potential. We fix the time at which the delta-function pulse is applied at  $t = 0$ . The corresponding vector potential is given by

$$A(t) = -A\theta(t). \quad (8)$$

One can expand the current measured at time  $t$  up to the first order with respect to  $A$ ,

$$j(t) = \int_{-\infty}^{\infty} d\bar{t} \left. \frac{\delta j(t)}{\delta A(\bar{t})} \right|_{A=0} A(\bar{t}) \quad (9)$$

We define the Fourier transform of  $j(t)$  as

$$j(\Omega) = \int_{-\infty}^{\infty} dt e^{i\Omega t} j(t). \quad (10)$$

Substituting Eq. (8) into Eq. (9) and using the relation ( $\eta$  is a positive infinitesimal constant),

$$\theta(t) = i \int_{-\infty}^{\infty} \frac{d\omega}{2\pi} \frac{e^{-i\omega t}}{\omega + i\eta}, \quad (11)$$

we obtain

$$\begin{aligned} j(\Omega) &= -iA \int_{-\infty}^{\infty} \frac{d\omega}{2\pi} \int_{-\infty}^{\infty} dt e^{i(\Omega-\omega)t} \frac{\chi^{(1)}(\omega)}{\omega + i\eta} \\ &= -iA \frac{\chi^{(1)}(\Omega)}{\Omega + i\eta} = A\sigma(\Omega). \end{aligned} \quad (12)$$

Thus, the linear response against the delta-function pulse (i.e., the broad-band limit) is also described by the optical conductivity spectrum. Note, however, that the meaning of  $\Omega$  is different between the two limits:  $\Omega$  is the frequency of the monochromatic wave in the narrow-band limit, while  $\Omega$  is the frequency of the Fourier transformed current in the broad-band limit.

In the following sections, the formalism can be straightforwardly extended to multi-pulse cases for the 2DCS, which can be generally represented by a complicated integral of higher-order correlation functions. In the narrow-band and broad-band limits, the expression is greatly simplified, and the 2DCS signal is directly related to certain nonlinear susceptibilities without the integral. Contrary to the case of the linear response, we will see that the two limits are described by different types of correlation functions.

### III. TWO-DIMENSIONAL COHERENT SPECTROSCOPY WITH GENERAL PULSES

Let us consider a general situation where the system is driven by two pulses with arbitrary wave forms. We call the first pulse injected into the system a ‘pulse 1’, and call the second one a ‘pulse 2’. The delay time between the two pulses is denoted by  $\tau$ . We show the time profile

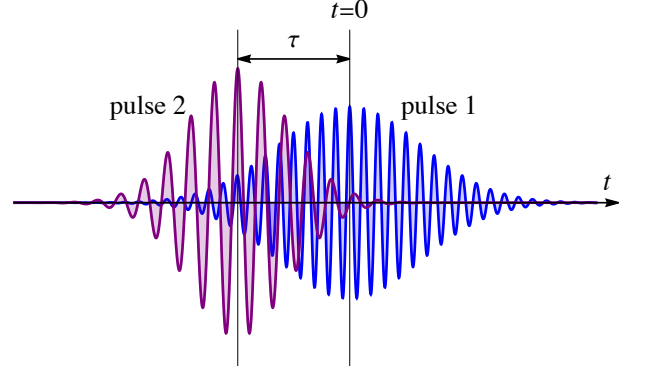


FIG. 1. Schematic picture of the configuration of two pulses with a time delay  $\tau$ .

of the two pulses in Fig. 1. The vector potential is written as

$$A(t) = A_1(t) + A_2(t + \tau), \quad (13)$$

where  $A_1(t)$  is the wave form of the pulse 1, and  $A_2(t)$  is the wave form of the pulse 2, which is shifted by the delay time  $\tau$ .

We define the current solely induced by the pulse  $i$  ( $= 1, 2$ ) as  $j_i(t)$ . That is, we turn off the other pulse and measure the current, which is expanded as a function of  $A_i(t)$  up to the third order. Since the second-order term is absent when the system has the inversion symmetry, the expansion of  $j_i(t)$  reads

$$\begin{aligned} j_i(t) &= \int_{-\infty}^{\infty} d\bar{t} \left. \frac{\delta j(t)}{\delta A(\bar{t})} \right|_{A=0} A_i(\bar{t} + \delta_{i,2}\tau) \\ &\quad + \frac{1}{3!} \int_{-\infty}^{\infty} d\bar{t} d\bar{t}' d\bar{t}'' \left. \frac{\delta^3 j(t)}{\delta A(\bar{t}) \delta A(\bar{t}') \delta A(\bar{t}'')} \right|_{A=0} \\ &\quad \times A_i(\bar{t} + \delta_{i,2}\tau) A_i(\bar{t}' + \delta_{i,2}\tau) A_i(\bar{t}'' + \delta_{i,2}\tau) \\ &\quad (i = 1, 2). \end{aligned} \quad (14)$$

We also define the total current induced by both the pulse 1 and pulse 2 as  $j_{12}(t)$ , which is expanded as

$$\begin{aligned} j_{12}(t) &= \int_{-\infty}^{\infty} d\bar{t} \left. \frac{\delta j(t)}{\delta A(\bar{t})} \right|_{A=0} (A_1(\bar{t}) + A_2(\bar{t} + \tau)) \\ &\quad + \frac{1}{3!} \int_{-\infty}^{\infty} d\bar{t} d\bar{t}' d\bar{t}'' \left. \frac{\delta^3 j(t)}{\delta A(\bar{t}) \delta A(\bar{t}') \delta A(\bar{t}'')} \right|_{A=0} \\ &\quad \times (A_1(\bar{t}) + A_2(\bar{t} + \tau)) (A_1(\bar{t}') + A_2(\bar{t}' + \tau)) \\ &\quad \times (A_1(\bar{t}'') + A_2(\bar{t}'' + \tau)). \end{aligned} \quad (15)$$

Now the nonlinear current is defined by subtracting  $j_1(t)$  and  $j_2(t)$  from  $j_{12}(t)$ ,

$$j_{\text{NL}}(t, \tau) = j_{12}(t) - j_1(t) - j_2(t), \quad (16)$$

which can be written as

$$\begin{aligned} j_{\text{NL}}(t, \tau) &= \frac{1}{2} \int_{-\infty}^{\infty} d\bar{t} d\bar{t}' d\bar{t}'' \left. \frac{\delta^3 j(t)}{\delta A(\bar{t}) \delta A(\bar{t}') \delta A(\bar{t}'')} \right|_{A=0} \\ &\quad \times (A_1(\bar{t}) A_1(\bar{t}') A_2(\bar{t}'' + \tau) \\ &\quad + A_1(\bar{t}) A_2(\bar{t}' + \tau) A_2(\bar{t}'' + \tau)). \end{aligned} \quad (17)$$

The nonlinear current is split into two parts: One is proportional to  $A_1^2 A_2$  and the other is proportional to  $A_1 A_2^2$ . Let us denote these terms as  $j_{A_1^2 A_2}(t, \tau)$  and  $j_{A_1 A_2^2}(t, \tau)$ , respectively, which can be distinguished from the intensity dependence of the two pulses.

We first look at the first part,  $j_{A_1^2 A_2}(t, \tau)$ , which can be double Fourier transformed as

$$j_{A_1^2 A_2}(\omega_t, \omega_\tau) = \int_{-\infty}^{\infty} dt e^{i\omega_t t} \int_{-\infty}^{\infty} d\tau e^{i\omega_\tau \tau} j_{A_1^2 A_2}(t, \tau). \quad (18)$$

By performing the  $\tau$  integral, we obtain

$$\begin{aligned} & j_{A_1^2 A_2}(\omega_t, \omega_\tau) \\ &= \frac{1}{2} \int_{-\infty}^{\infty} dt e^{i\omega_t t} \int_{-\infty}^{\infty} d\bar{t} d\bar{t}' d\bar{t}'' \frac{\delta^3 j(t)}{\delta A(\bar{t}) \delta A(\bar{t}') \delta A(\bar{t}'')} \Big|_{A=0} \\ & \times \int_{-\infty}^{\infty} \frac{d\omega}{2\pi} \int_{-\infty}^{\infty} \frac{d\omega'}{2\pi} e^{-i(\omega \bar{t} + \omega' \bar{t}' + \omega_\tau \bar{t}'')} \\ & \times A_1(\omega) A_1(\omega') A_2(\omega_\tau) \end{aligned} \quad (19)$$

Now we rewrite the above expression using the third-order current correlation function defined by

$$\begin{aligned} & \chi^{(3)}(\Omega; \Omega_1, \Omega_2, \Omega_3) \\ &= \frac{1}{3!} \int_{-\infty}^{\infty} d\bar{t} d\bar{t}' d\bar{t}'' e^{i\Omega \bar{t} - i(\Omega_1 \bar{t} + \Omega_2 \bar{t}' + \Omega_3 \bar{t}'')} \\ & \times \frac{\delta^3 j(t)}{\delta A(\bar{t}) \delta A(\bar{t}') \delta A(\bar{t}'')} \Big|_{A=0} \quad (\Omega = \Omega_1 + \Omega_2 + \Omega_3). \end{aligned} \quad (20)$$

Note that the right-hand side of Eq. (20) does not depend on  $t$  due to the time-translation symmetry. The correlation function  $\chi^{(3)}(\Omega; \Omega_1, \Omega_2, \Omega_3)$  is invariant under the exchange of  $\Omega_i$  and  $\Omega_j$  ( $i \neq j$ ).

Using  $\chi^{(3)}$ , we can express Eq. (19) as

$$\begin{aligned} j_{A_1^2 A_2}(\omega_t, \omega_\tau) &= 3A_2(\omega_\tau) \int_{-\infty}^{\infty} \frac{d\omega}{2\pi} A_1(\omega) A_1(\omega_t - \omega_\tau - \omega) \\ & \times \chi^{(3)}(\omega_t; \omega, \omega_t - \omega_\tau - \omega, \omega_\tau). \end{aligned} \quad (21)$$

This is the general formula that we derive for the 2DCS signal proportional to  $A_1^2 A_2$ . Since  $A_2(\omega_\tau)$  is factored out of the integral in Eq. (21), the signal is enhanced along the horizontal line in the two-dimensional frequency space where  $\omega_\tau$  is close to the central frequency of the spectrum  $A_2(\omega)$ . A similar formula can be derived for the signal proportional to  $A_1 A_2^2$ ,

$$\begin{aligned} j_{A_1 A_2^2}(\omega_t, \omega_\tau) &= 3A_1(\omega_t - \omega_\tau) \int_{-\infty}^{\infty} \frac{d\omega}{2\pi} A_2(\omega) A_2(\omega_\tau - \omega) \\ & \times \chi^{(3)}(\omega_t; \omega, \omega_\tau - \omega, \omega_t - \omega_\tau). \end{aligned} \quad (22)$$

In this case,  $A_1(\omega_t - \omega_\tau)$  is factored out, meaning that the signal is enhanced along the line parallel to the diagonal line where  $\omega_t - \omega_\tau$  is close to the central frequency of the spectrum  $A_1(\omega)$ .

We notice that there is a symmetry between Eq. (21) and Eq. (22) through the relation,

$$j_{A_1^2 A_2}(\omega_t, \omega_\tau) = j_{A_2 A_1^2}(\omega_t, \omega_t - \omega_\tau). \quad (23)$$

Thus,  $j_{A_1^2 A_2}$  and  $j_{A_1 A_2^2}$  essentially contain the same information. If the pulse 1 and pulse 2 have the same wave form (i.e.,  $A_1(t) = A_2(t)$ ), then the nonlinear current,  $j_{\text{NL}}(\omega_t, \omega_\tau) = j_{A_1^2 A_2}(\omega_t, \omega_\tau) + j_{A_1 A_2^2}(\omega_t, \omega_\tau)$ , has the reflection symmetry,

$$j_{\text{NL}}(\omega_t, \omega_\tau) = j_{\text{NL}}(\omega_t, \omega_t - \omega_\tau). \quad (24)$$

From Eqs. (21) and (22), we can see that the 2DCS signal is given by a frequency integral of the third-order nonlinear susceptibility multiplied by the Fourier spectra of the pulse fields  $A_1$  and  $A_2$ . By engineering the wave form and choosing an appropriate combination of the frequencies  $\omega_t$  and  $\omega_\tau$ , one can extract the information of certain part of  $\chi^{(3)}(\Omega; \Omega_1, \Omega_2, \Omega_3)$ . Below we study two particular cases, the narrow-band and broad-band limits, where the 2DCS signal is most directly related to  $\chi^{(3)}$  without the frequency integral.

#### IV. TWO-DIMENSIONAL COHERENT SPECTROSCOPY IN THE NARROW-BAND LIMIT

In this section, we focus on the narrow-band limit, that is, the two pulses are both monochromatic waves with infinitely large pulse widths (we sometimes call those driving fields as pulses, even though the pulse widths are diverging). In general, the two driving fields can have different frequencies. Here we limit ourselves to the case in which the two pulses have the same frequency  $\Omega$ , which allows us to write down the 2DCS signal in a simple form. The corresponding vector potential reads

$$\begin{aligned} A(t) &= A_1(t) + A_2(t + \tau) \\ &= A_1 \cos(\Omega t) + A_2 \cos(\Omega(t + \tau)), \end{aligned} \quad (25)$$

where the pulse 1 has an amplitude  $A_1$ , and the pulse 2 has an amplitude  $A_2$  with the delay time  $\tau$ . Since we consider nonlinear responses, we include both  $+\Omega$  and  $-\Omega$  components (i.e.,  $\cos \Omega t = \frac{1}{2}(e^{i\Omega t} + e^{-i\Omega t})$ ) in the vector potential. The corresponding Fourier spectra of the pulse fields are given by

$$A_1(\omega) = \pi A_1 (\delta(\omega - \Omega) + \delta(\omega + \Omega)), \quad (26)$$

$$A_2(\omega) = \pi A_2 (\delta(\omega - \Omega) + \delta(\omega + \Omega)). \quad (27)$$

Using the formula (21), we obtain the 2DCS signal

proportional to  $A_1^2 A_2$  in the narrow-band limit,

$$\begin{aligned}
 j_{A_1^2 A_2}(\omega_t, \omega_\tau) &= \frac{3}{2} \pi^2 A_1^2 A_2 \left[ \delta(\omega_t - 3\Omega) \delta(\omega_\tau - \Omega) \chi^{(3)}(3\Omega; \Omega, \Omega, \Omega) \right. \\
 &\quad + \delta(\omega_t - \Omega) (2\delta(\omega_\tau - \Omega) + \delta(\omega_\tau + \Omega)) \\
 &\quad \times \chi^{(3)}(\Omega; \Omega, \Omega, -\Omega) \\
 &\quad + \delta(\omega_t + \Omega) (2\delta(\omega_\tau + \Omega) + \delta(\omega_\tau - \Omega)) \\
 &\quad \times \chi^{(3)}(-\Omega; \Omega, -\Omega, -\Omega) \\
 &\quad \left. + \delta(\omega_t + 3\Omega) \delta(\omega_\tau + \Omega) \chi^{(3)}(-3\Omega; -\Omega, -\Omega, -\Omega) \right]. \quad (28)
 \end{aligned}$$

In the same way, the signal proportional to  $A_1 A_2^2$  can be derived from Eq. (22) as

$$\begin{aligned}
 j_{A_1 A_2^2}(\omega_t, \omega_\tau) &= \frac{3}{2} \pi^2 A_1 A_2^2 \\
 &\quad \times \left[ \delta(\omega_t - 3\Omega) \delta(\omega_\tau - 2\Omega) \chi^{(3)}(3\Omega; \Omega, \Omega, \Omega) \right. \\
 &\quad + \delta(\omega_t - \Omega) (2\delta(\omega_\tau) + \delta(\omega_\tau - 2\Omega)) \chi^{(3)}(\Omega; \Omega, \Omega, -\Omega) \\
 &\quad + \delta(\omega_t + \Omega) (2\delta(\omega_\tau) + \delta(\omega_\tau + 2\Omega)) \chi^{(3)}(-\Omega; \Omega, -\Omega, -\Omega) \\
 &\quad \left. + \delta(\omega_t + 3\Omega) \delta(\omega_\tau + 2\Omega) \chi^{(3)}(-3\Omega; -\Omega, -\Omega, -\Omega) \right]. \quad (29)
 \end{aligned}$$

One can see that the 2DCS signal  $j_{\text{NL}}(\omega_t, \omega_\tau) = j_{A_1^2 A_2}(\omega_t, \omega_\tau) + j_{A_1 A_2^2}(\omega_t, \omega_\tau)$  only appears at several discrete spots. The components at  $(\omega_t/\Omega, \omega_\tau/\Omega) = (3, 2), (3, 1), (-3, -1), (-3, -2)$  are proportional to  $\chi^{(3)}(3\Omega; \Omega, \Omega, \Omega)$  (or  $\chi^{(3)}(-3\Omega; -\Omega, -\Omega, -\Omega)$ ), which corresponds to the third harmonic generation. On the other hand, the components at  $(\omega_t/\Omega, \omega_\tau/\Omega) = (1, 2), (1, 1), (1, 0), (1, -1), (-1, 1), (-1, 0), (-1, -1), (-1, -2)$  are proportional to  $\chi^{(3)}(\Omega; \Omega, \Omega, -\Omega)$  (or  $\chi^{(3)}(-\Omega; \Omega, -\Omega, -\Omega)$ ), which is the susceptibility of the ac Kerr effect. Hence, the 2DCS in the narrow-band limit is fully characterized by the THG and ac Kerr susceptibilities, as pointed out previously. In the literature of 2DCS [6], the signals at  $(\omega_t, \omega_\tau) = (\Omega, -\Omega), (\Omega, 0), (\Omega, \Omega), (\Omega, 2\Omega)$  are referred to as rephasing, pump-probe, non-rephasing, and two-quantum responses, respectively. We summarize the results in the two-dimensional map shown in Fig. 2. In this way, with the measurement of the 2DCS one can extract the third-order nonlinear component at the fundamental frequency  $\Omega$  without being disturbed by the dominant linear response component having the same frequency  $\Omega$ .

## V. TWO-DIMENSIONAL COHERENT SPECTROSCOPY IN THE BROAD-BAND LIMIT

Next, let us consider the opposite limit, i.e., the broad-band limit, in the 2DCS. As in the case of the linear

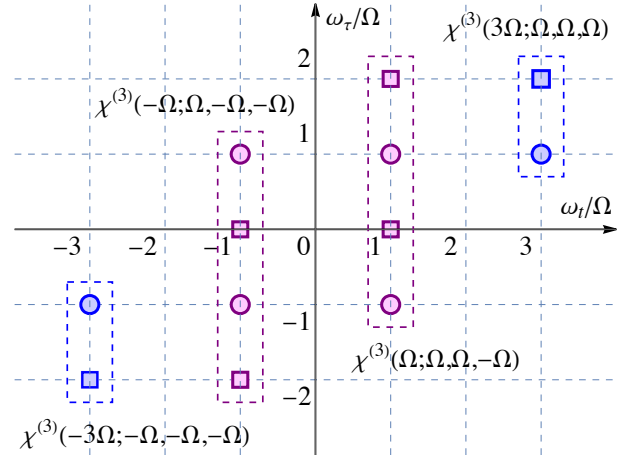


FIG. 2. 2DCS spectrum  $j_{\text{NL}}(\omega_t, \omega_\tau)$  in the narrow-band limit. The circles represent the signals proportional to  $A_1^2 A_2$ , while the squares represent the signals proportional to  $A_1 A_2^2$ . The blue and purple markers correspond to the third harmonic generation and ac Kerr susceptibilities, respectively.

response, the broad-band pulses are modeled by delta-functions,

$$E(t) = A_1 \delta(t) + A_2 \delta(t + \tau), \quad (30)$$

where the pulse 1 is centered at  $t = 0$ , and the pulse 2 is centered at  $t = -\tau$ . The corresponding vector potential is given by  $A(t) = A_1(t) + A_2(t + \tau) = -A_1 \theta(t) - A_2 \theta(t + \tau)$ . The Fourier transform of  $A_i(t)$  ( $i = 1, 2$ ) reads

$$A_1(\omega) = -\frac{iA_1}{\omega + i\eta}, \quad (31)$$

$$A_2(\omega) = -\frac{iA_2}{\omega + i\eta}. \quad (32)$$

From Eq. (21), we can evaluate the 2DCS signal proportional to  $A_1^2 A_2$  in the broad-band limit,

$$\begin{aligned}
 j_{A_1^2 A_2}(\omega_t, \omega_\tau) &= \frac{3(-i)^3}{\omega_\tau + i\eta} A_1^2 A_2 \int_{-\infty}^{\infty} \frac{d\omega}{2\pi} \frac{1}{\omega + i\eta} \frac{1}{\omega_t - \omega_\tau - \omega + i\eta} \\
 &\quad \times \chi^{(3)}(\omega_t; \omega, \omega_t - \omega_\tau - \omega, \omega_\tau). \quad (33)
 \end{aligned}$$

We can further simplify the expression to get

$$\begin{aligned}
 j_{A_1^2 A_2}(\omega_t, \omega_\tau) &= \frac{6(-i)^3}{(\omega_\tau + i\eta)(\omega_t - \omega_\tau + 2i\eta)} A_1^2 A_2 \\
 &\quad \times \int_{-\infty}^{\infty} \frac{d\omega}{2\pi} \frac{1}{\omega + i\eta} \chi^{(3)}(\omega_t; \omega, \omega_t - \omega_\tau - \omega, \omega_\tau). \quad (34)
 \end{aligned}$$

From Eq. (34), we notice that the signal diverges along the diagonal ( $\omega_t = \omega_\tau$ ) and horizontal ( $\omega_\tau = 0$ ) lines. In Fig. 3, we show the diverging region in the two-dimensional frequency space. In particular, along the

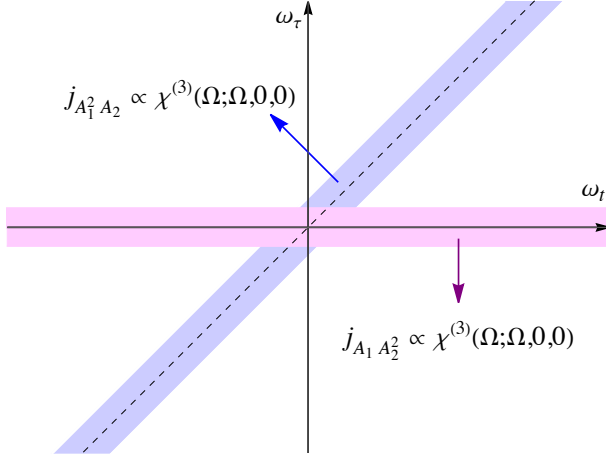


FIG. 3. 2DCS spectrum  $j_{\text{NL}}(\omega_t, \omega_\tau)$  in the broad-band limit. The signal is diverging along the diagonal ( $\omega_t = \omega_\tau$ ) and horizontal ( $\omega_\tau = 0$ ) lines.  $j_{A_1^2 A_2}$  along the diagonal line and  $j_{A_1 A_2^2}$  along the horizontal line are proportional to the dc Kerr susceptibility.

diagonal line ( $\omega_t = \omega_\tau = \Omega$ ) the signal  $j_{A_1^2 A_2}(\omega_t, \omega_\tau)$  apart from the divergent factor  $\frac{1}{\omega_t - \omega_\tau + 2i\eta}$  has a simple expression. To see this, let us write

$$j_{A_1^2 A_2}(\Omega, \Omega) \propto \frac{6(-i)^3 A_1^2 A_2}{\Omega} \int_{-\infty}^{\infty} \frac{d\omega}{2\pi} \frac{1}{\omega + i\eta} \chi^{(3)}(\Omega; \omega, -\omega, \Omega). \quad (35)$$

Using the relation  $\frac{1}{\omega + i\eta} = \mathcal{P} \frac{1}{\omega} - i\pi\delta(\omega)$  ( $\mathcal{P}$  indicates the principal value) and noticing that  $\chi^{(3)}(\Omega; \omega, -\omega, \Omega)$  is an even function of  $\omega$ , we have

$$j_{A_1^2 A_2}(\Omega, \Omega) \propto \frac{3A_1^2 A_2}{\Omega} \chi^{(3)}(\Omega; \Omega, 0, 0). \quad (36)$$

Thus, we find that the 2DCS signal proportional to  $A_1^2 A_2$  along the diagonal line is described by  $\chi^{(3)}(\Omega; \Omega, 0, 0)$ , which corresponds to the susceptibility for the dc Kerr effect. This result is in sharp contrast to the case of the narrow-band limit, where the 2DCS signal is given by  $\chi^{(3)}(\Omega; \Omega, \Omega, \Omega)$  and  $\chi^{(3)}(\Omega; \Omega, \Omega, -\Omega)$  (Sec. IV). The lesson from this is that the 2DCS signal is related to different nonlinear susceptibilities depending on the width of the pulses (narrow-band or broad-band pulses).

A similar formula can be derived for the 2DCS signal proportional to  $A_1 A_2^2$  with the formula (22). The result is

$$\begin{aligned} j_{A_1 A_2^2}(\omega_t, \omega_\tau) &= \frac{6(-i)^3}{(\omega_\tau + i\eta)(\omega_t - \omega_\tau + 2i\eta)} A_1 A_2^2 \\ &\times \int_{-\infty}^{\infty} \frac{d\omega}{2\pi} \frac{1}{\omega + i\eta} \chi^{(3)}(\omega_t; \omega, \omega_\tau - \omega, \omega_t - \omega_\tau). \end{aligned} \quad (37)$$

Again, the signal is divergent along the diagonal ( $\omega_t = \omega_\tau$ ) and horizontal ( $\omega_\tau = 0$ ) lines. In the case of  $j_{A_1 A_2^2}$ ,

further simplification occurs along the horizontal line. In fact, at  $\omega_t = \Omega$  and  $\omega_\tau = 0$  the susceptibility  $\chi^{(3)}(\omega_t; \omega_t - \omega_\tau, \omega, \omega_\tau - \omega)$  becomes an even function of  $\omega$ , with which the  $\omega$  integral can be performed analytically. Apart from the diverging factor  $\frac{1}{\omega_\tau + i\eta}$ , the 2DCS signal is given by

$$j_{A_1 A_2^2}(\Omega, 0) \propto \frac{3A_1 A_2^2}{\Omega} \chi^{(3)}(\Omega; \Omega, 0, 0). \quad (38)$$

We find that the 2DCS signal proportional to  $A_1 A_2^2$  along the horizontal line is described by the dc Kerr susceptibility  $\chi^{(3)}(\Omega; \Omega, 0, 0)$ .

If we add the contributions proportional to  $A_1^2 A_2$  and  $A_1 A_2^2$ , we obtain the expression for the total nonlinear current along the diagonal line,

$$\begin{aligned} j_{\text{NL}}(\Omega, \Omega) &\propto \frac{3}{\Omega} (A_1^2 A_2 + A_1 A_2^2) \chi^{(3)}(\Omega; \Omega, 0, 0) \\ &+ \frac{6(-i)^3}{\Omega} A_1 A_2^2 \\ &\times \mathcal{P} \int_{-\infty}^{\infty} \frac{d\omega}{2\pi} \frac{1}{\omega} \chi^{(3)}(\Omega; \omega, \Omega - \omega, 0), \end{aligned} \quad (39)$$

and along the horizontal line,

$$\begin{aligned} j_{\text{NL}}(\Omega, 0) &\propto \frac{3}{\Omega} (A_1^2 A_2 + A_1 A_2^2) \chi^{(3)}(\Omega; \Omega, 0, 0) \\ &+ \frac{6(-i)^3}{\Omega} A_1^2 A_2 \\ &\times \mathcal{P} \int_{-\infty}^{\infty} \frac{d\omega}{2\pi} \frac{1}{\omega} \chi^{(3)}(\Omega; \omega, \Omega - \omega, 0). \end{aligned} \quad (40)$$

Here we have the frequency integral of the third-order nonlinear susceptibility on top of the dc Kerr susceptibility.

To summarize, the 2DCS in the broad-band limit has divergent signals along the diagonal and horizontal lines. If one keeps track of the intensity dependence ( $A_1^2 A_2$  or  $A_1 A_2^2$ ), the signal is proportional to the dc Kerr susceptibility  $\chi^{(3)}(\Omega; \Omega, 0, 0)$ . For other regions in the two-dimensional frequency space, the signal is described by the complicated integral of the third-order nonlinear susceptibility (see the formulas (34) and (37)). In the next section, we numerically evaluate the ac and dc Kerr susceptibilities for a model of disordered superconductors.

## VI. NUMERICAL SIMULATION

### A. Model

In the previous sections, we have seen that the 2DCS signals in the narrow-band and broad-band limits are related to the ac and dc Kerr susceptibilities ( $\chi^{(3)}(\Omega; \Omega, \Omega, -\Omega)$  and  $\chi^{(3)}(\Omega; \Omega, 0, 0)$ ). In this section, we evaluate them numerically for a lattice model of dis-

ordered superconductors. The Hamiltonian is defined by

$$\hat{H}(t) = \sum_{\mathbf{k}, \sigma} \epsilon_{\mathbf{k}-\mathbf{A}(t)} c_{\mathbf{k}\sigma}^\dagger c_{\mathbf{k}\sigma} - \frac{V}{N} \sum_{\mathbf{k}, \mathbf{k}'} c_{\mathbf{k}\uparrow}^\dagger c_{-\mathbf{k}\downarrow}^\dagger c_{-\mathbf{k}'\downarrow} c_{\mathbf{k}'\uparrow} + \sum_{i, \sigma} v_i c_{i\sigma}^\dagger c_{i\sigma}, \quad (41)$$

where  $c_{\mathbf{k}\sigma}^\dagger$  is the creation operator of electrons with momentum  $\mathbf{k}$  and spin  $\sigma$ ,  $\epsilon_{\mathbf{k}}$  is the band dispersion,  $V(>0)$  is the attractive interaction strength,  $N$  is the number of  $k$  points, and  $v_i$  is a local random potential at site  $i$ .

We assume the BCS pairing interaction in the  $s$ -wave channel, for which we employ the mean-field approximation to decompose the interaction term. The gap function is defined by

$$\Delta(t) = -\frac{V}{N} \sum_{\mathbf{k}} \langle c_{-\mathbf{k}\downarrow}(t) c_{\mathbf{k}\uparrow}(t) \rangle. \quad (42)$$

Without loss of generality, we take  $\Delta(t)$  to be a real value. The disorder potential  $v_i$  is assumed to be a Gaussian random variable with the disorder average,  $\langle v_i v_j \rangle_{\text{disorder}} = \gamma^2 \delta_{ij}$ . Here  $\gamma$  is the average impurity scattering rate. Within the self-consistent Born approximation, the effect of the disorder is included in the form of the self-energy [50, 58],

$$\Sigma(t, t') = \frac{\gamma^2}{N} \sum_{\mathbf{k}} G_{\mathbf{k}}(t, t'), \quad (43)$$

where  $G_{\mathbf{k}}(t, t')$  is the single-particle Green's function in the Keldysh formalism [59, 60]. In Appendix A, we briefly summarize the Keldysh formalism for the Green's function.

In our numerical simulation, we consider the square lattice with the dispersion  $\epsilon_{\mathbf{k}} = -2t_h(\cos k_x + \cos k_y)$  ( $t_h$  is the hopping amplitude and we set the lattice constant  $a = 1$ ), which has the inversion symmetry. We use  $t_h$  as the unit of energy, and set  $t_h = 1$  throughout the paper. The pulse field is assumed to be polarized along the  $x$  axis (i.e.,  $\mathbf{e} = (1, 0)$ ). The number of particles is fixed at half filling (the chemical potential is set to  $\mu = 0$ ). The number of  $k$  points used in this paper is taken to be  $N = 100 \times 100$ . We confirm that the results do not change even if we increase  $N$  up to  $200 \times 200$ . We use the interaction parameter  $V = 2.5$ , and take a small imaginary part  $\eta = 0.01$  as a broadening factor for the Green's function and nonlinear susceptibilities.

We solve the Green's function self-consistently within the BCS and self-consistent Born approximations. The nonlinear susceptibilities are systematically derived by differentiating the current,

$$j(t) = \sum_{\mathbf{k}\sigma\mu} e_\mu \frac{\partial \epsilon_{\mathbf{k}-\mathbf{A}(t)}}{\partial k_\mu} \langle c_{\mathbf{k}\sigma}^\dagger(t) c_{\mathbf{k}\sigma}(t) \rangle, \quad (44)$$

with respect to the driving field  $A(t)$ . The derivation is analogous to that of the third harmonic generation

TABLE I. Classification of the third-order nonlinear susceptibility diagrams for disordered superconductors within the self-consistent Born approximation (see also Appendix C and Table II in Ref. [50]). The second column shows the number of photon lines attached to each vertex, while the third column shows the type of the coupling to electromagnetic fields. For the Higgs-mode contributions, the vertices are split into two groups separated by the Higgs-mode propagator.

label	number of photons	coupling
QP1	4	diamag
QP2	3 + 1	paramag
QP3	2 + 2	diamag
QP4	2 + 1 + 1	diamag + paramag
QP5	1 + 1 + 1 + 1	paramag
H1	(2) + (2)	diamag
H2	(2) + (1 + 1)	diamag + paramag
H3	(1 + 1) + (1 + 1)	paramag

[50, 52]. The nonlinear susceptibility is subject to the impurity and Higgs-mode vertex corrections, which should be included consistently with the form of the self-energy. The details of the impurity and Higgs-mode vertices are summarized in Appendix B. The explicit form of the nonlinear susceptibilities is given in Appendix C.

The nonlinear susceptibility diagrams for disordered superconductors are classified according to the number of photon lines attached to each vertex as shown in Table I (see also Appendix C and Ref. [50]). There are five types of diagrams assigned to the contribution of quasiparticles and three types of diagrams assigned to the Higgs-mode contribution. For the latter, the photon vertices are split into two groups separated by the Higgs-mode propagator. Within the self-consistent Born approximation, the inversion symmetry is effectively recovered if the original system without disorders has the inversion symmetry. In this case, the number of photon lines in each group must be even since vertices with the odd number of photons are parity odd and the momentum integral of an odd parity function vanishes. For example, grouping such as (3) + (1), (2 + 1) + (1), and (1 + 1 + 1) + (1) does not appear for the Higgs-mode diagram in Table I. The coupling to electric fields is either diamagnetic or paramagnetic depending on an even or odd number of photons attached to the vertex. In the study of third harmonic generation, it has been known that the diagrams with the paramagnetic coupling become dominant over those with the diamagnetic coupling if the system is in the dirty regime. We will see that similar behavior is observed for the 2DCS signal.

## B. Results

Let us first look at the equilibrium and linear-response spectra for our model. Figure 4 shows the single-particle spectrum  $A(\omega)$  in the superconducting phase of the lat-



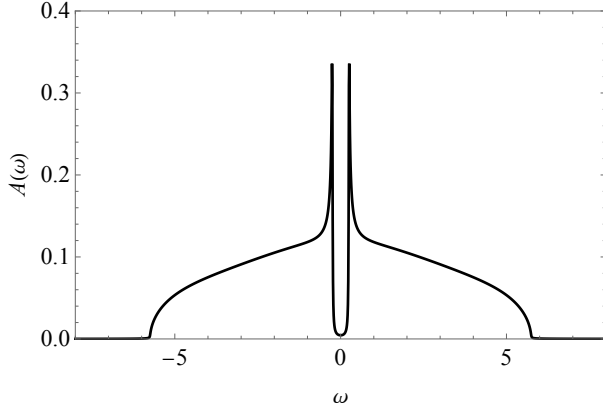


FIG. 4. Single-particle spectrum in the superconducting phase of the lattice model in the dirty regime. The parameters are  $V = 2.5$ ,  $\gamma = 2$ , and  $\beta = 50$ . The gap size is  $2\Delta = 0.50$  and  $\gamma/(2\Delta) = 4.0$ .

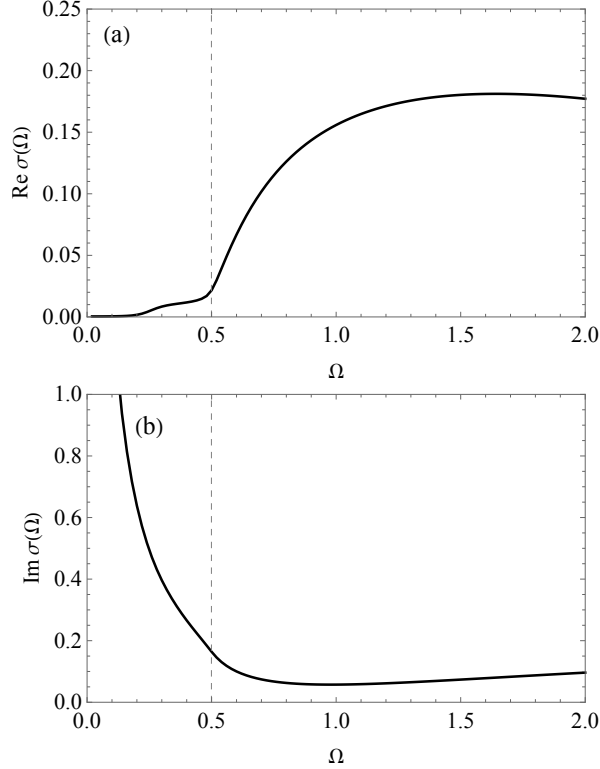


FIG. 5. (a) Real and (b) imaginary parts of the optical conductivity  $\sigma(\Omega)$  in the superconducting phase of the lattice model in the dirty regime. The parameters are  $V = 2.5$ ,  $\gamma = 2$ , and  $\beta = 50$ . The dashed lines indicate the gap frequency  $2\Delta = 0.50$ .

tice model with  $V = 2.5$ ,  $\gamma = 2$ , and the inverse temperature  $\beta = 50$ . As we will see below, the superconducting transition temperature is  $T_c \approx 0.14$  ( $\beta_c \approx 7.1$ ) in this case, so that the system is in the superconducting phase. In the single-particle spectrum, we can see that a gap is opening with  $2\Delta = 0.50$  at  $\beta = 50$ . This means

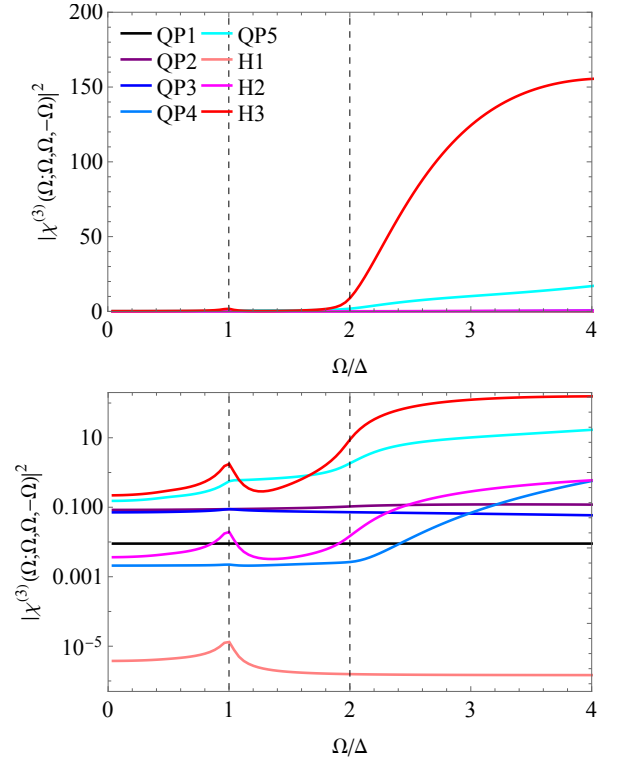


FIG. 6. Intensity of the ac Kerr susceptibility  $\chi^{(3)}(\Omega; \Omega, \Omega, -\Omega)$  as a function of  $\Omega/\Delta$  in the linear scale (top panel) and log scale (bottom) in the superconducting phase of the lattice model in the dirty regime. The parameters are  $V = 2.5$ ,  $\gamma = 2$ , and  $\beta = 50$ . The dashed lines indicate  $\Omega = \Delta$  and  $\Omega = 2\Delta$ .

that the system is in the dirty regime ( $\gamma/(2\Delta) = 4.0$ ). We can confirm that the relation (1) is roughly satisfied ( $W = 8$ ,  $\gamma = 2$ ,  $2\Delta = 0.50$ ,  $v_F/L = 0.02$ ).

In Fig. 5, we plot the optical conductivity  $\sigma(\Omega)$  for the same parameter set. The real part [Fig. 5(a)] shows a build-up of the spectral weight above the gap frequency, resembling the Mattis-Bardeen form of the optical conductivity in the dirty limit [46]. The result is consistent with the fact that the system is in the dirty regime ( $\gamma/(2\Delta) = 4.0$ ). The tiny spectral weight below the gap is due to the presence of the small broadening factor ( $\eta = 0.01$ ) in the Green's function. The imaginary part [Fig. 5] shows a  $1/\Omega$  divergence at low frequency, which signals a nonzero superfluid stiffness.

We then move on to see the ac Kerr susceptibility  $\chi^{(3)}(\Omega; \Omega, \Omega, -\Omega)$ , which describes the 2DCS signal in the narrow-band limit (Sec. IV). In Fig. 6, we plot  $|\chi^{(3)}(\Omega; \Omega, \Omega, -\Omega)|^2$  as a function of  $\Omega/\Delta$  in the linear scale (top panel) and log scale (bottom) in the superconducting phase of the lattice model ( $V = 2.5$ ,  $\gamma = 2$ , and  $\beta = 50$ ). We classify the contribution into eight different diagrams (QP1, ..., QP5, H1, ..., H3) as in Table I. We can see that  $\chi^{(3)}(\Omega; \Omega, \Omega, -\Omega)$  shows threshold behavior in the linear scale, i.e., the spectral weight starts to grow at the gap frequency  $\Omega = 2\Delta$  as  $\Omega$  in-



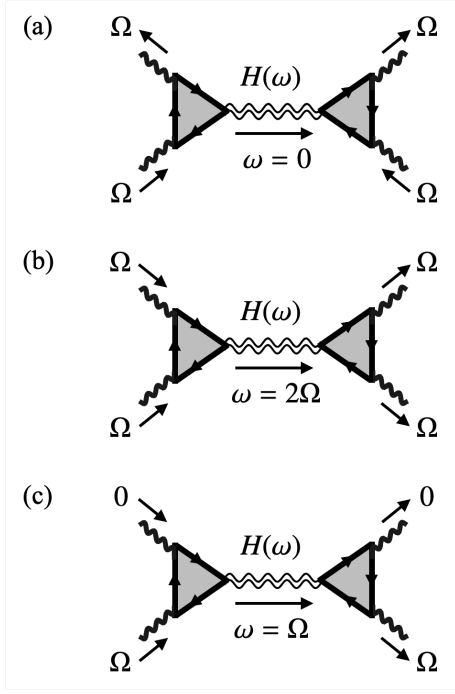


FIG. 7. H3 diagrams for [(a), (b)] the ac Kerr susceptibility  $\chi^{(3)}(\Omega; \Omega, \Omega, -\Omega)$  with the Higgs-mode propagator  $H(\omega)$  (double wavy lines) carrying frequency (a)  $\omega = 0$  and (b)  $\omega = 2\Omega$ , and (c) the dc Kerr susceptibility  $\chi^{(3)}(\Omega; \Omega, 0, 0)$ . The single wavy lines and solid lines represent the photon propagators and electron propagators, respectively, while the shaded triangles indicate electron loop diagrams including impurity corrections.

creases. This is in contrast to the previous argument [38] that  $\chi^{(3)}(\Omega; \Omega, \Omega, -\Omega)$  could be resonantly enhanced at  $\Omega = 2\Delta$ . We attribute this to the difference of the treatments of disorders (see the discussion in Sec. I). The dominant contribution at  $\Omega \geq 2\Delta$  is coming from the Higgs mode with the paramagnetic coupling (H3 diagram). The second dominant contribution is from the QP5 diagram (i.e., quasiparticles with the paramagnetic coupling to single photons). The other diagrams have much smaller weights with the difference of several orders of magnitude. This is similar to the behavior of third harmonic generation that shows resonance at  $\Omega = \Delta$  [30, 50]. The THG susceptibility is also dominated by the Higgs mode in the dirty regime.

The interpretation of these results is as follows: The H3 diagrams for  $\chi^{(3)}(\Omega; \Omega, \Omega, -\Omega)$  are shown in Fig. 7(a) and (b) depending on the combination of the in-coming and out-going photons. For  $\Omega \geq 2\Delta$ , the main contribution comes from the diagram (a), since (b) is suppressed due to high frequency ( $2\Omega \geq 4\Delta$ ) carried by the Higgs-mode propagator. In Fig. 7(a), the Higgs mode carries zero frequency, meaning that the process is far off-resonant (recall that the eigenfrequency of the Higgs mode at zero momentum is  $2\Delta$ ). Thus, the ac Kerr susceptibility in charge of the 2DCS in the narrow-band limit

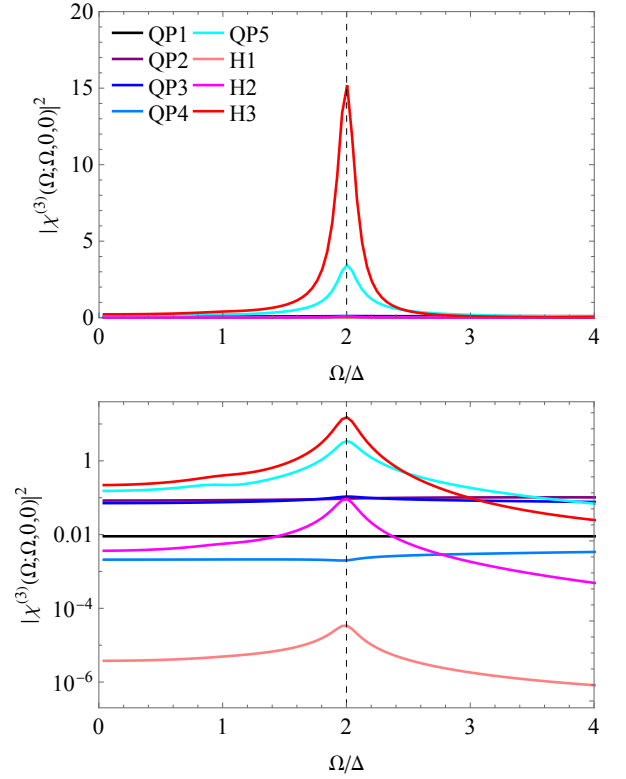


FIG. 8. Intensity of the dc Kerr susceptibility  $\chi^{(3)}(\Omega; \Omega, 0, 0)$  as a function of  $\Omega/\Delta$  in the linear scale (top panel) and log scale (bottom) in the superconducting phase of the lattice model in the dirty regime. The parameters are  $V = 2.5$ ,  $\gamma = 2$ , and  $\beta = 50$ . The dashed lines indicate  $\Omega = 2\Delta$ .

is mainly mediated by the zero-frequency ( $\omega = 0$ ) Higgs mode, picking up the tail of the Higgs-mode resonance peak centered at  $\omega = 2\Delta$ . This scenario is similar to the one employed for the pump-probe spectroscopy of superconductors in the clean regime [12, 28]. The ac Kerr susceptibility physically describes the modulation of the optical response by external pump light  $A_{\text{pump}}$  ( $\delta\chi^{(1)}(\Omega) \sim \chi^{(3)}(\Omega; \Omega, \Omega, -\Omega)A_{\text{pump}}^2$ ). Since  $\chi^{(1)}(\Omega) = i\Omega\sigma(\Omega)$  has threshold behavior at  $\omega = 2\Delta$  in the dirty regime,  $\chi^{(3)}(\Omega; \Omega, \Omega, -\Omega)$  inherits similar frequency dependence.

If we look at the log-scale plot of  $|\chi^{(3)}(\Omega; \Omega, \Omega, -\Omega)|^2$  (bottom panel of Fig. 6), we notice that there is a tiny resonance peak at  $\Omega = \Delta$  (half of the gap frequency), which is the same resonance frequency as in THG. This resonance is also dominated by the H3 diagram, and can be simply explained by the two-photon absorption process (see also Ref. [61]). As shown in Fig. 7(b), the Higgs mode can carry the frequency  $\omega = 2\Omega$  due to two-photon absorption, and resonance occurs at  $\Omega = \Delta$ , where  $2\Omega$  agrees with the eigenfrequency of the Higgs mode. This is similar to the story of the THG resonance observed at  $\Omega = \Delta$ , in which the H3 diagram also plays the dominant role.

Next, let us examine the numerical results for the

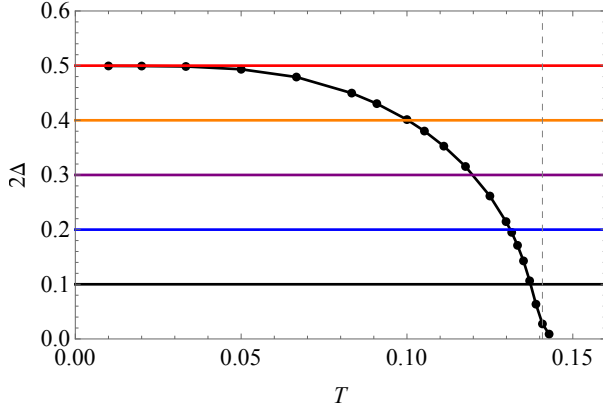


FIG. 9. Temperature dependence of the superconducting gap  $2\Delta$  for the lattice model with  $V = 2.5$  and  $\gamma = 2$ . The dashed line shows the critical temperature  $T_c \approx 0.14$ . The horizontal lines represent constant frequencies  $\Omega = 0.1, 0.2, \dots, 0.5$ .

dc Kerr susceptibility  $\chi^{(3)}(\Omega; \Omega, 0, 0)$ , which is related to the 2DCS signal along the diagonal and horizontal lines in the broad-band limit (Sec. V). In Fig. 8, we plot  $|\chi^{(3)}(\Omega; \Omega, 0, 0)|^2$  as a function of  $\Omega/\Delta$  in the linear scale (top panel) and log scale (bottom) in the superconducting phase of the lattice model ( $V = 2.5$ ,  $\gamma = 2$ , and  $\beta = 50$ ). We decompose the contribution into different diagrams (QP1, ..., QP5, H1, ..., H3 as in Table I). We can observe that the dc Kerr susceptibility shows a resonance peak at  $\Omega = 2\Delta$ , which is dominated by the H3 diagram. The second largest contribution comes from the QP5 diagram. The fact that the H3 diagram plays a dominant role is similar to the case of the ac Kerr susceptibility (Fig. 6) and THG susceptibility [50] in the dirty regime of superconducting systems. The reason that the resonance appears at  $\Omega = 2\Delta$  can be understood from the H3 diagram shown in Fig. 7(c). In the case of the dc Kerr effect, there are an in-coming photon with frequency  $\Omega$  and another in-coming photon with zero frequency. In total, the Higgs-mode propagator carries the fundamental driving frequency  $\Omega$ , with which the resonance occurs when  $\Omega$  agrees with the eigenfrequency of the Higgs mode  $2\Delta$ . Thus, the frequency dependence of the 2DCS signal may become qualitatively different between the narrow-band and broad-band limit: In the former, the signal grows towards high frequencies with the threshold  $\Omega = 2\Delta$ . In the latter, the signal along the diagonal and horizontal lines is partly described by the dc Kerr susceptibility, which shows the resonance peak at  $\Omega = 2\Delta$ . In realistic situations, the behavior of the 2DCS signal will be in between the narrow-band and broad-band limits, which may help to understand the experimental results.

To get closer to experiments, we study the temperature dependence of the ac and dc Kerr susceptibilities of disordered superconductors. In Fig. 9, we show the temperature dependence of the equilibrium superconducting gap  $2\Delta$  for  $V = 2.5$  and  $\gamma = 2$ . The gap grows below the critical temperature  $T_c \approx 0.14$ . We overlay constant fre-

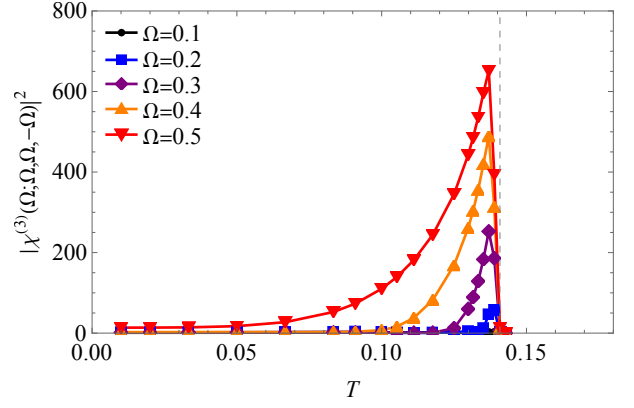


FIG. 10. Temperature dependence of the ac Kerr susceptibility  $\chi^{(3)}(\Omega; \Omega, \Omega, -\Omega)$  at  $\Omega = 0.1, 0.2, \dots, 0.5$  for the lattice model with  $V = 2.5$  and  $\gamma = 2$ . The dashed line shows the critical temperature  $T_c \approx 0.14$ .

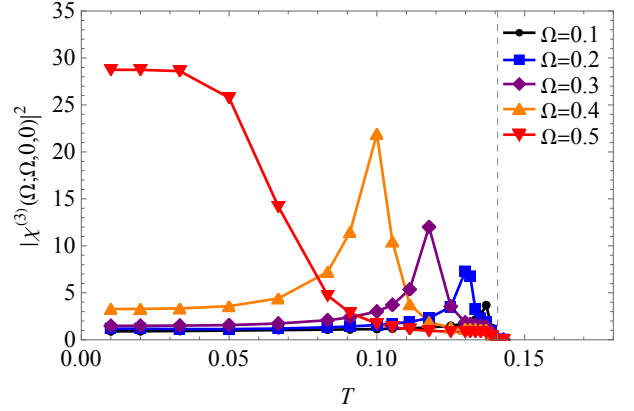


FIG. 11. Temperature dependence of the dc Kerr susceptibility  $\chi^{(3)}(\Omega; \Omega, \Omega, 0, 0)$  at  $\Omega = 0.1, 0.2, \dots, 0.5$  for the lattice model with  $V = 2.5$  and  $\gamma = 2$ . The dashed line shows the critical temperature  $T_c \approx 0.14$ .

quency lines  $\Omega = 0.1, 0.2, \dots, 0.5$  in Fig. 9. The crossing between the  $2\Delta$  curve and horizontal lines corresponds to the point where  $\Omega = 2\Delta$  is fulfilled.

In Fig. 10, we plot the temperature dependence of the intensity of the ac Kerr susceptibility  $|\chi^{(3)}(\Omega; \Omega, \Omega, -\Omega)|^2$  at  $\Omega = 0.1, 0.2, \dots, 0.5$ . As temperature decreases, the susceptibility sharply develops at  $T = T_c$ , and then gradually decreases toward low temperature. There seems to be a peak in the temperature profile, but this is not caused by resonance (if any). In fact, the peak position does not change as  $\Omega$  is varied but stays in the vicinity of  $T_c$  irrespective of  $\Omega$ . This behavior can be understood from the previous observation that the ac Kerr susceptibility has the threshold at  $\Omega = 2\Delta$ . When temperature decreases below  $T_c$ , the spectral weight of  $\chi^{(3)}(\Omega; \Omega, \Omega, -\Omega)$  rapidly builds up for a wide range of  $\Omega$ . As temperature goes down further, there appears a spectral gap at  $\Omega \leq 2\Delta$ . If we fix  $\Omega$  and decrease  $T$ , the ac Kerr susceptibility gets suppressed when  $2\Delta(T) \geq \Omega$

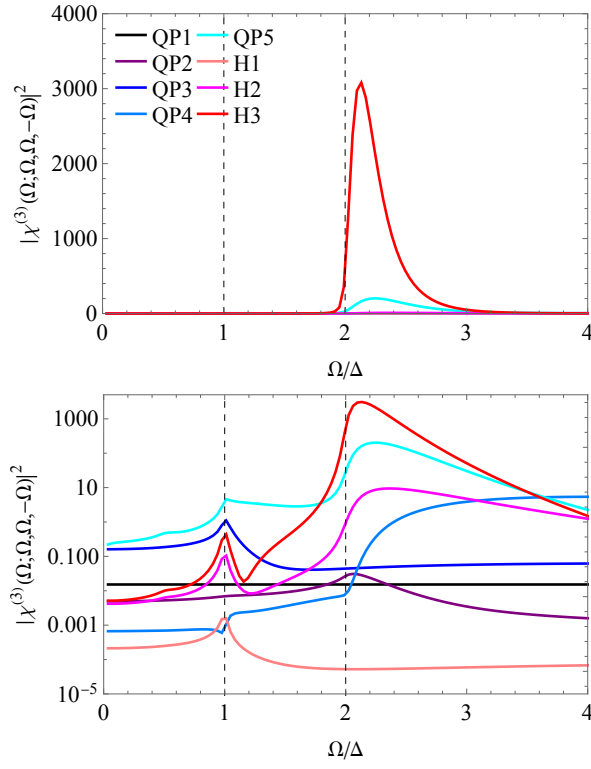


FIG. 12. Intensity of the ac Kerr susceptibility  $\chi^{(3)}(\Omega; \Omega, \Omega, -\Omega)$  as a function of  $\Omega/\Delta$  in the linear scale (top panel) and log scale (bottom) in the superconducting phase of the lattice model in the clean regime. The parameters are  $V = 2.5$ ,  $\gamma = 0.5$ , and  $\beta = 50$ . The dashed lines indicate  $\Omega = \Delta$  and  $\Omega = 2\Delta$ .

(see Fig. 9), explaining the behavior of  $\chi^{(3)}(\Omega; \Omega, \Omega, -\Omega)$  at low temperature.

In Fig. 11, we plot the temperature dependence of the intensity of the dc Kerr susceptibility  $|\chi^{(3)}(\Omega; \Omega, 0, 0)|^2$  at  $\Omega = 0.1, 0.2, \dots, 0.5$ , which shows peaks well below  $T_c$ . In contrast to the case of the ac Kerr susceptibility (Fig. 10), the peak position clearly depends on  $\Omega$ . By comparing with the temperature dependent gap size (Fig. 9), we can see that the peak position corresponds to the resonance condition  $\Omega = 2\Delta$ . As we have seen in Fig. 8, the dc Kerr susceptibility  $\chi^{(3)}(\Omega; \Omega, 0, 0)$  has the resonance at  $\Omega = 2\Delta$ , which is also observed in the temperature profile. The result is reminiscent of the experimental observation of the 2DCS signals for NbN superconductors, where similar resonance structure emerges at  $\Omega = 2\Delta$ . Although these experimental results were obtained for narrow-band pulses, they may contain some part of the dc Kerr effect, since the pulses used in the experiment have finite bandwidth and are in between the narrow-band and broad-band limits. To establish tight connection to experiments, we need to evaluate the full 2DCS signals, which requires complicated calculations of the integral of the third-order nonlinear susceptibilities with different combination of frequencies (Eqs. (39) and (40)).

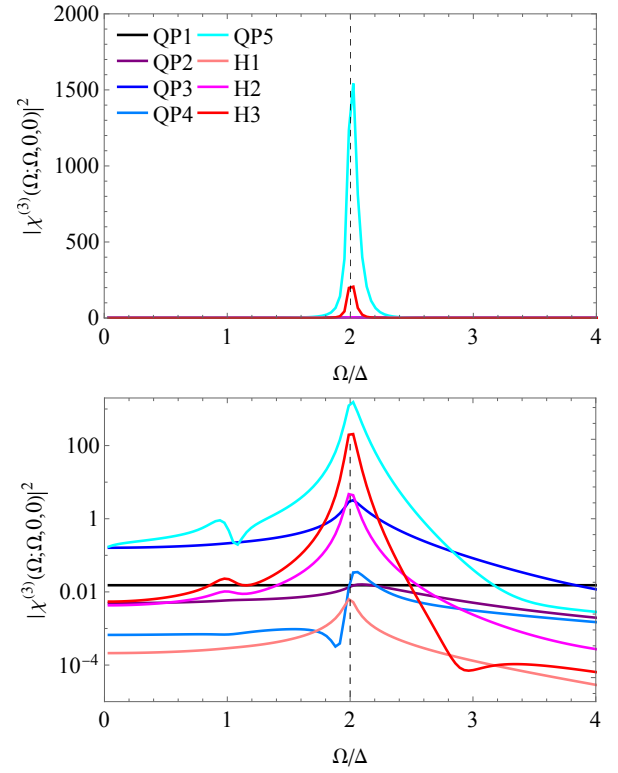


FIG. 13. Intensity of the dc Kerr susceptibility  $\chi^{(3)}(\Omega; \Omega, 0, 0)$  as a function of  $\Omega/\Delta$  in the linear scale (top panel) and log scale (bottom) in the superconducting phase of the lattice model in the clean regime. The parameters are  $V = 2.5$ ,  $\gamma = 0.5$ , and  $\beta = 50$ . The dashed lines indicate  $\Omega = \Delta$  and  $\Omega = 2\Delta$ .

Finally, we investigate the impurity dependence of the ac and dc Kerr susceptibilities. As shown for THG, the nonlinear susceptibilities strongly depends on the strength of the impurity scattering  $\gamma$ . Depending on the value of  $\gamma$ , there always arises competition between the Higgs mode and quasiparticle excitations for those non-linear processes. Here we take  $\gamma = 0.5$ , which is smaller than that for the previous calculations ( $\gamma = 2$ ), and the other parameters remain to be the same ( $V = 2.5$  and  $\beta = 50$  as in Figs. 6 and 8). In this parameter set, the gap size is  $2\Delta = 1.1$  and  $\gamma/(2\Delta) = 0.45$ , which means that the system is in the clean regime.

In Fig. 12, we plot  $|\chi^{(3)}(\Omega; \Omega, \Omega, -\Omega)|^2$  for  $\gamma = 0.5$ . As compared to the one for  $\gamma = 2$  (Fig. 6), the susceptibility still shows the threshold behavior at  $\Omega = 2\Delta$  dominated by the H3 diagram. The difference is that we can see the decay of the ac Kerr susceptibility at high frequencies within the plot region. In the clean limit ( $\gamma \rightarrow 0$ ), the paramagnetic coupling should disappear, and the contribution of the H3 diagram will vanish. Thus, we expect that the ac Kerr susceptibility decays more rapidly if we further decrease the value of  $\gamma$ , and the weight at  $\Omega \geq 2\Delta$  is strongly suppressed. The resonance at  $\Omega = \Delta$ , on the other hand, is dominated by the quasiparticle contributions (mainly coming from the QP5 and QP3 diagrams).

TABLE II. The relation between the 2DCS in the narrow-band and broad-band limits and third-order nonlinear susceptibilities at selected frequencies. We restrict ourselves to the case of non-negative frequencies ( $\omega_t, \omega_\tau \geq 0$ ), and decompose the 2DCS signal into those proportional to  $A_1^2 A_2$  and  $A_1 A_2^2$  in the broad-band limit. For each susceptibility, we show characteristic behavior and the dominant physical origin (Higgs mode or quasiparticles) in the clean and dirty regimes.

pulse	frequency	nonlinear susceptibility	behavior	clean	dirty
narrow band	$(\omega_t, \omega_\tau) = (3\Omega, \Omega), (3\Omega, 2\Omega)$	THG: $\chi^{(3)}(3\Omega; \Omega, \Omega, \Omega)$	resonance at $\Omega = \Delta$	quasiparticles	Higgs
	$(\omega_t, \omega_\tau) = (\Omega, 0), (\Omega, \Omega), (\Omega, 2\Omega)$	ac Kerr: $\chi^{(3)}(\Omega; \Omega, \Omega, -\Omega)$	threshold at $\Omega = 2\Delta$	Higgs (off-resonant)	Higgs (off-resonant)
broad band	$(\omega_t, \omega_\tau) = (\Omega, \Omega) (j \propto A_1^2 A_2)$	dc Kerr: $\chi^{(3)}(\Omega; \Omega, 0, 0)$	resonance at $\Omega = \Delta$	quasiparticles	Higgs
	$(\omega_t, \omega_\tau) = (\Omega, 0) (j \propto A_1 A_2^2)$		resonance at $\Omega = 2\Delta$	quasiparticles	Higgs

As in THG, we expect that the two-photon absorption resonance will survive in the clean limit, and is governed by quasiparticle excitations.

In Fig. 13, we plot  $|\chi^{(3)}(\Omega; \Omega, 0, 0)|^2$  for  $\gamma = 0.5$ . We again find the resonance peak at  $\Omega = 2\Delta$ , which is dominated by the quasiparticle contributions mainly coming from QP5 diagram. We also notice that the weight of the QP3 diagram is enhanced around  $\Omega = 2\Delta$ . In the clean limit, the paramagnetic coupling to electromagnetic fields disappears, and the resonance at  $\Omega = 2\Delta$  in the dc Kerr effect will be governed by the quasiparticles with the diamagnetic coupling.

The results are summarized in Table II. Although the ac Kerr susceptibility at  $\Omega \geq 2\Delta$  is dominated by the Higgs mode both in the clean and dirty regimes, it only shows the threshold behavior, and the Higgs mode is far off-resonant. The dc Kerr susceptibility, on the other hand, shows resonance at  $\Omega = 2\Delta$ , which is dominated by the Higgs mode in the dirty regime. However, there is a competition between the Higgs mode and quasiparticles depending on the disorder strength as in THG [47–51]. In this regard, 2DCS has similar issues on identifying the physical origin of the peak as THG. There always exists a possibility that the quasiparticle excitations contribute to the resonance at  $\Omega = 2\Delta$ . We cannot clearly distinguish the contribution of quasiparticles from that of the Higgs mode only by looking at experimental data of the frequency or temperature dependence of 2DCS. One needs to compare experimental results with theoretical calculations to understand the origin of the 2DCS signal.

On the other hand, 2DCS may contain different information than THG. The 2DCS signal is related to the ac and dc Kerr susceptibilities in the narrow-band and broad-band limits. More generally, the 2DCS can be described by the integral of the third-order nonlinear susceptibility with different frequency combinations (Eqs. (39) and (40)). Thus, we can use 2DCS to reconstruct third-order nonlinear susceptibilities that are otherwise hard to access by other methods.

## VII. SUMMARY AND OUTLOOK

To summarize, we have studied the behavior of the two-dimensional coherent spectroscopy (2DCS) for disordered superconductors in the narrow-band and broad-band limits. We first derive the general formulas (Eqs. (39) and (40)) that relate the 2DCS signal with the third-order nonlinear susceptibility for general pulse forms (not limited to the narrow-band and broad-band limits). Then, we apply the formulas to the narrow-band and broad-band limits. In the former, the 2DCS signal is described by the THG and ac Kerr susceptibilities ( $\chi^{(3)}(3\Omega; \Omega, \Omega, \Omega)$  and  $\chi^{(3)}(\Omega; \Omega, \Omega, -\Omega)$ ) as in previous studies. In the latter, we show that the 2DCS signal diverges along the diagonal and horizontal lines in the two-dimensional frequency space. We decompose the diverging signal into two components according to the pulse amplitude dependence ( $A_1^2 A_2$  or  $A_1 A_2^2$ ). We find that one of the components is directly proportional to the dc Kerr susceptibility  $\chi^{(3)}(\Omega; \Omega, 0, 0)$ .

Based on these, we have performed numerical calculations of the ac and dc Kerr susceptibilities for a lattice model of disordered superconductors within the BCS and self-consistent Born approximations. We demonstrate that the ac Kerr susceptibility shows the threshold behavior at  $\Omega = 2\Delta$  rather than resonant enhancement. This is natural since the ac Kerr susceptibility probes the modulation of the linear optical response, which shows the threshold at  $\Omega = 2\Delta$ . The main contribution to the ac Kerr susceptibility comes from the Higgs-mode diagram. However, the Higgs mode mediating the ac Kerr effect carries zero frequency. Hence the signal only picks up the zero-frequency tail of the Higgs-mode peak (i.e., far off-resonance process). The dc Kerr susceptibility, on the other hand, shows a clear resonance peak at  $\Omega = 2\Delta$ , which is also dominated by the Higgs mode in the dirty regime. In this case, the signal arises from the resonant process with the Higgs mode, where one in-coming photon carries the fundamental frequency  $\Omega$  and another in-coming photon carries zero frequency. We summarize the results in Table II.

We have also studied the temperature dependence of the ac and dc Kerr susceptibilities. In both cases, peaks

appear in the temperature profile. In the case of the ac Kerr susceptibility, the peak position does not depend on the pulse frequency but stays close to the critical temperature. This reflects the threshold behavior that the spectral weight starts to grow above the gap frequency. In contrast, the dc Kerr susceptibility exhibits a peak that is always located at  $\Omega = 2\Delta$ . This mainly arises due to the resonance with the Higgs mode in the dirty regime. The disorder-strength dependence suggests that there is a competition between the Higgs-mode and quasiparticle contributions as is the case for THG (see Table II). As we approach the clean limit, the quasiparticle excitations give dominant contributions to the resonance peak of the dc Kerr susceptibility at  $\Omega = 2\Delta$ . For the ac Kerr susceptibility, the Higgs mode continues to contribute significantly even in the clean regime. We expect that the signal is eventually dominated by quasiparticles in the clean limit, since the paramagnetic coupling to electromagnetic fields vanishes in that limit and the remaining QP3 diagram has much larger contribution than the H1 diagram having the diamagnetic coupling.

Let us comment on the relevance of the present results with the experiment [38]. As mentioned previously, the experimentally observed peak in the 2DCS signal at  $\Omega = 2\Delta$  for NbN superconductors is similar to the behavior of the dc Kerr susceptibility rather than the ac Kerr susceptibility. For the latter, we show that the peak in the temperature profile should appear in the vicinity of  $T_c$  rather than the point where  $\Omega = 2\Delta(T)$  is satisfied. Thus, the argument based on the ac Kerr susceptibility cannot explain the experimental results. We think that in realistic situations the 2DCS signal contains some part of the contribution of the dc Kerr susceptibility, since laser pulses used in experiments have finite bandwidth, which is in between the narrow-band and broad-band limits. To fully understand the experimental results, we need to evaluate the integral of the third-order nonlinear susceptibility with different frequency combinations, which we leave as a future problem. Let us emphasize that quasiparticles always compete with the Higgs mode in 2DCS (as in THG, see Table II). In particular, the resonance peak in the dc Kerr susceptibility is dominated by quasiparticles in the clean regime. Thus, the 2DCS alone does not discriminate the Higgs-mode contribution. One has

to compare experimental results with theoretical calculations to see the physical origin of the 2DCS signal.

Finally, we discuss several open issues related to the present work. First, we have focused on the narrow-band and broad-band limits in 2DCS in this paper. In the broad-band limit, we further restrict ourselves to the diverging part along the diagonal and horizontal lines in the two-dimensional frequency plane. To obtain the full two-dimensional map of the coherent spectroscopy for general pulse wave forms, one has to evaluate the integral of the third-order nonlinear susceptibility using Eqs. (39) and (40). While this can be accessible within the present formalism, numerical cost is more demanding. Second, the effect of strong disorders beyond the self-consistent Born approximation has not been well understood. As we have mentioned before, one has to take large system size to keep the scale separation [Eq. (1)]. One possible approach is to take account of maximally crossed diagrams ('Cooperon diagrams') for disorders, which are relevant for weak localization effects [57, 62]. Third, one has to consider multiorbital effects to understand the difference of the experimental observation of 2DCS for NbN and MgB<sub>2</sub> [38, 39]. For the latter, there has not been observed a peak in the temperature profile of the 2DCS signal. Since MgB<sub>2</sub> is a typical multi-gap superconductor, the role of another collective mode, the Leggett mode [48, 63–69], in 2DCS should be understood from microscopic calculations. More exotic collective modes in superconductors, such as the Higgs mode with unconventional pairing symmetries [70–74] and the Bardasis-Schrieffer mode [75] are also the target of the future study of 2DCS.

## ACKNOWLEDGMENTS

We would like to thank N. P. Armitage, K. Katsumi, D. Manske, S. Neri, R. Shimano, and P. Werner for fruitful discussions. N.T. acknowledges support by JSPS KAKENHI (Grant Nos. JP24H00191, JP25H01246, and JP25H01251) and JST FOREST (Grant No. JP-MJFR2131).

## Appendix A: Keldysh formalism

In this Appendix, we briefly summarize the Keldysh formalism of Green's functions used in the calculation of the nonlinear susceptibilities for disordered superconductors. We define the retarded, advanced, and lesser components of the Green's function as follows:

$$G_{\mathbf{k}}^R(t, t') = -i\theta(t - t')\langle\{\psi_{\mathbf{k}}(t), \psi_{\mathbf{k}}^\dagger(t')\}\rangle, \quad (\text{A1})$$

$$G_{\mathbf{k}}^A(t, t') = i\theta(t' - t)\langle\{\psi_{\mathbf{k}}(t), \psi_{\mathbf{k}}^\dagger(t')\}\rangle, \quad (\text{A2})$$

$$G_{\mathbf{k}}^<(t, t') = i\langle\psi_{\mathbf{k}}^\dagger(t')\psi_{\mathbf{k}}(t)\rangle. \quad (\text{A3})$$

Here  $\psi_{\mathbf{k}}(t) = (c_{\mathbf{k}\uparrow}(t), c_{-\mathbf{k}\downarrow}^\dagger(t))^T$  is the Nambu spinor, and each Green's function is in the form of a  $2 \times 2$  matrix in the Nambu space. For the lattice model with the Hamiltonian (41), the Green's functions are determined within the

BCS and self-consistent Born approximations as

$$G_{\mathbf{k}}^{R-1}(\omega) = \omega + i\eta + \mu - \epsilon_{\mathbf{k}}\tau_3 - \Delta\tau_1 - \frac{\gamma^2}{N} \sum_{\mathbf{k}} \tau_3 G_{\mathbf{k}}^R(\omega) \tau_3, \quad (\text{A4})$$

$$G_{\mathbf{k}}^A(\omega) = [G_{\mathbf{k}}^R(\omega)]^\dagger, \quad (\text{A5})$$

$$G_{\mathbf{k}}^<(\omega) = f(\omega)[G_{\mathbf{k}}^A(\omega) - G_{\mathbf{k}}^R(\omega)]. \quad (\text{A6})$$

In the above,  $\tau_i$  ( $i = 1, 2, 3$ ) are Pauli matrices, and  $f(\omega) = 1/(e^{\beta\omega} + 1)$  is the Fermi-Dirac distribution with inverse temperature  $\beta$ . Since  $G_{\mathbf{k}}^R(\omega)$  appears on both sides of Eq. (A4), one has to solve it iteratively until convergence is reached. The gap function  $\Delta$  is determined from the gap equation (42), which is written in terms of the Green's function as

$$\Delta = i \frac{V}{2} \int \frac{d\omega}{2\pi} \frac{1}{N} \sum_{\mathbf{k}} \text{Tr}[\tau_1 G_{\mathbf{k}}^<(\omega)]. \quad (\text{A7})$$

We numerically solve Eqs. (A4)-(A7) self-consistently.

The optical conductivity can be calculated through Eq. (4) with

$$\chi^{(1)}(\Omega) = i \int \frac{d\omega}{2\pi} \frac{1}{N} \sum_{\mathbf{k}} \text{Tr}[\ddot{\epsilon}_{\mathbf{k}} \tau_3 G_{\mathbf{k}}(\omega)]^< + i \int \frac{d\omega}{2\pi} \frac{1}{N} \sum_{\mathbf{k}} \text{Tr}[\dot{\epsilon}_{\mathbf{k}} G_{\mathbf{k}}(\omega) \dot{\epsilon}_{\mathbf{k}} G_{\mathbf{k}}(\omega)]^<. \quad (\text{A8})$$

Here we use the notation of the Langreth rule [60, 76] (i.e.,  $[GG]^< = G^R G^< + G^< G^A$ ), and  $\ddot{\epsilon}_{\mathbf{k}} = \sum_{\mu\nu} \frac{\partial^2 \epsilon_{\mathbf{k}}}{\partial k_\mu \partial k_\nu} e_\mu e_\nu$  and  $\dot{\epsilon}_{\mathbf{k}} = \sum_{\mu} \frac{\partial \epsilon_{\mathbf{k}}}{\partial k_\mu} e_\mu$  are the derivatives of the band dispersion ( $e_\mu$  is the polarization vector of driving pulses). Note that there is no impurity and Higgs-mode vertex correction in  $\chi^{(1)}(\Omega)$ .

## Appendix B: Impurity and Higgs-mode vertices

In this Appendix, we show the self-consistent equations for the impurity and Higgs-mode vertices that are necessary in calculating the third-order susceptibility for 2DCS. Those equations are efficiently derived by differentiating the Dyson equation (A4) with respect to the driving field as many times as one needs. The derivatives of the self-energy part turn into the vertex corrections. The derived equations are a simple extension of those for the third harmonic generation as detailed in Ref. [50].

The impurity and Higgs-mode vertices are classified according to the type of the coupling to the electric field: One is the diamagnetic coupling ( $\mathbf{A}^2$ ) and the other is the paramagnetic coupling ( $\mathbf{j} \cdot \mathbf{A}$ ). When calculating linear and nonlinear susceptibilities within the self-consistent Born approximation, one has to include all the noncrossing impurity diagrams that are not contained in the Green's function, which forms a series of ladder diagrams. For the diamagnetic coupling, the impurity vertex  $\Lambda_{\alpha\beta}^{\text{dia}}(\omega; \Omega)$  satisfies the following equation,

$$\Lambda_{\alpha\beta}^{\text{dia}}(\omega; \Omega) = \frac{\gamma^2}{N} \sum_{\mathbf{k}} \tau_3 G_{\mathbf{k}}(\omega + (\alpha + \beta)\Omega) \ddot{\epsilon}_{\mathbf{k}} \tau_3 G_{\mathbf{k}}(\omega) \tau_3 + \frac{\gamma^2}{N} \sum_{\mathbf{k}} \tau_3 G_{\mathbf{k}}(\omega) \Lambda_{\alpha\beta}^{\text{dia}}(\omega + (\alpha + \beta)\Omega) G_{\mathbf{k}}(\omega) \tau_3, \quad (\text{B1})$$

with  $\alpha, \beta = 1, 0, -1$ . Here the total frequency injected at the diamagnetic vertex is given by  $(\alpha + \beta)\Omega$ . We omit the Keldysh labels ( $R, A, <$ ) for simplicity, but it should be understood according to the Langreth rule [60, 76]. By solving Eq. (B1) iteratively, one can include all the impurity ladder corrections to the diamagnetic bare vertex. Similarly, we have the self-consistent equation for the paramagnetic impurity vertex  $\Lambda_{\alpha\beta}^{\text{para}}(\omega; \Omega)$ ,

$$\begin{aligned} \Lambda_{\alpha\beta}^{\text{para}}(\omega; \Omega) &= \frac{\gamma^2}{N} \sum_{\mathbf{k}} \tau_3 G_{\mathbf{k}}(\omega + (\alpha + \beta)\Omega) (\dot{\epsilon}_{\mathbf{k}} G_{\mathbf{k}}(\omega + \alpha\Omega) \dot{\epsilon}_{\mathbf{k}} + \dot{\epsilon}_{\mathbf{k}} G_{\mathbf{k}}(\omega + \beta\Omega) \dot{\epsilon}_{\mathbf{k}}) G_{\mathbf{k}}(\omega) \tau_3 \\ &+ \frac{\gamma^2}{N} \sum_{\mathbf{k}} \tau_3 G_{\mathbf{k}}(\omega + (\alpha + \beta)\Omega) \Lambda_{\alpha\beta}^{\text{para}}(\omega; \Omega) G_{\mathbf{k}}(\omega) \tau_3. \end{aligned} \quad (\text{B2})$$

In the case of the paramagnetic coupling, the frequency injected at each paramagnetic vertex is given by  $\alpha\Omega$  and  $\beta\Omega$  ( $\alpha, \beta = 1, 0, -1$ ).

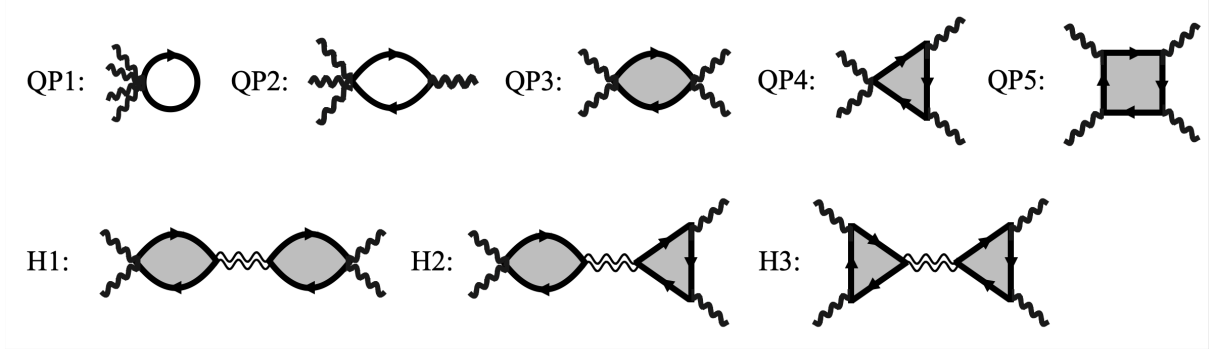


FIG. 14. Third-order susceptibility diagrams for disordered superconductors within the self-consistent Born approximation (see also Table II in Ref. [50]). The single wavy lines, double wavy lines, and solid lines represent the photon, Higgs-mode, and electron propagators, respectively. The shaded triangles and boxes indicate electron loop diagrams including impurity corrections. The labels QP1, ..., QP5 denote the quasiparticle contributions, while H1, ..., H3 denote the Higgs-mode contributions.

The  $\tau_1$  vertex (denoted by  $\Lambda_{\alpha\beta}^{\tau_1}(\omega; \Omega)$ ), responsible for the Higgs mode propagation, is also subject to the impurity corrections, satisfying the following equation:

$$\Lambda_{\alpha\beta}^{\tau_1}(\omega; \Omega) = \tau_1 + \frac{\gamma^2}{N} \sum_{\mathbf{k}} \tau_3 G_{\mathbf{k}}(\omega + (\alpha + \beta)\Omega) \Lambda_{\alpha\beta}^{\tau_1}(\omega; \Omega) G_{\mathbf{k}}(\omega) \tau_3. \quad (\text{B3})$$

Using the  $\tau_1$  vertex and impurity vertex, we can write down the self-consistent equation for the second derivative of the gap function with respect to the vector potential in the diamagnetic channel as

$$\ddot{\Delta}_{\alpha\beta}^{\text{dia}}(\Omega) = \frac{i}{2} \frac{V}{N} \sum_{\mathbf{k}} \int \frac{d\omega}{2\pi} \text{Tr}[\tau_1 G_{\mathbf{k}}(\omega + (\alpha + \beta)\Omega) (\ddot{\epsilon}_{\mathbf{k}} \tau_3 + \Lambda_{\alpha\beta}^{\text{dia}}(\omega; \Omega) + \Lambda_{\alpha\beta}^{\tau_1}(\omega; \Omega) \ddot{\Delta}_{\alpha\beta}^{\text{dia}}(\Omega)) G_{\mathbf{k}}(\omega)]^<, \quad (\text{B4})$$

and in the paramagnetic channel as

$$\begin{aligned} \ddot{\Delta}_{\alpha\beta}^{\text{para}}(\Omega) = & \frac{i}{2} \frac{V}{N} \sum_{\mathbf{k}} \int \frac{d\omega}{2\pi} \text{Tr}[\tau_1 G_{\mathbf{k}}(\omega + (\alpha + \beta)\Omega) (\dot{\epsilon}_{\mathbf{k}} G_{\mathbf{k}}(\omega + \alpha\Omega) \dot{\epsilon}_{\mathbf{k}} + \dot{\epsilon}_{\mathbf{k}} G_{\mathbf{k}}(\omega + \beta\Omega) \dot{\epsilon}_{\mathbf{k}} + \Lambda_{\alpha\beta}^{\text{para}}(\omega; \Omega) \\ & + \Lambda_{\alpha\beta}^{\tau_1}(\omega; \Omega) \ddot{\Delta}_{\alpha\beta}^{\text{para}}(\Omega)) G_{\mathbf{k}}(\omega)]^<. \end{aligned} \quad (\text{B5})$$

### Appendix C: Third-order nonlinear susceptibility for 2DCS

In this Appendix, we give the explicit form of the third-order nonlinear susceptibility for 2DCS. As we discussed in Sec. IV and V, the signals of the 2DCS in the narrow-band and broad-band limits are related to  $\chi^{(3)}(\Omega; +\Omega, +\Omega, -\Omega)$  and  $\chi^{(3)}(\Omega; \Omega, 0, 0)$ , respectively. In both cases, the susceptibility is decomposed into the quasiparticle and Higgs-mode contributions, each of which is further classified according to the topology of the corresponding diagrams. We show the classified diagrams in Fig. 14 (see also Table I in the main text).

For each diagram, we write down the explicit expression of the ac Kerr susceptibility using the Green's function









$$\begin{aligned}
\chi_{\text{QP5}}^{(3)}(\Omega; \Omega, 0, 0) = & \frac{i}{3} \int \frac{d\omega}{2\pi} \frac{1}{N} \sum_{\mathbf{k}} \text{Tr}[G_{\mathbf{k}}(\omega + \Omega) \dot{\epsilon}_{\mathbf{k}} G_{\mathbf{k}}(\omega) \dot{\epsilon}_{\mathbf{k}} G_{\mathbf{k}}(\omega) \dot{\epsilon}_{\mathbf{k}} G_{\mathbf{k}}(\omega)]^< \\
& + \frac{i}{3} \int \frac{d\omega}{2\pi} \frac{1}{N} \sum_{\mathbf{k}} \text{Tr}[G_{\mathbf{k}}(\omega + \Omega) \dot{\epsilon}_{\mathbf{k}} G_{\mathbf{k}}(\omega + \Omega) \dot{\epsilon}_{\mathbf{k}} G_{\mathbf{k}}(\omega) \dot{\epsilon}_{\mathbf{k}} G_{\mathbf{k}}(\omega)]^< \\
& + \frac{i}{3} \int \frac{d\omega}{2\pi} \frac{1}{N} \sum_{\mathbf{k}} \text{Tr}[G_{\mathbf{k}}(\omega + \Omega) \dot{\epsilon}_{\mathbf{k}} G_{\mathbf{k}}(\omega + \Omega) \dot{\epsilon}_{\mathbf{k}} G_{\mathbf{k}}(\omega + \Omega) \dot{\epsilon}_{\mathbf{k}} G_{\mathbf{k}}(\omega)]^< \\
& + \frac{i}{6} \int \frac{d\omega}{2\pi} \frac{1}{N} \sum_{\mathbf{k}} \text{Tr}[G_{\mathbf{k}}(\omega + \Omega) \dot{\epsilon}_{\mathbf{k}} G_{\mathbf{k}}(\omega) \Lambda_{0,0}^{\text{para}}(\omega; \Omega) G_{\mathbf{k}}(\omega)]^< \\
& + \frac{i}{3} \int \frac{d\omega}{2\pi} \frac{1}{N} \sum_{\mathbf{k}} \text{Tr}[G_{\mathbf{k}}(\omega + \Omega) \dot{\epsilon}_{\mathbf{k}} G_{\mathbf{k}}(\omega + \Omega) \Lambda_{1,0}^{\text{para}}(\omega; \Omega) G_{\mathbf{k}}(\omega)]^< \\
& + \frac{i}{6} \int \frac{d\omega}{2\pi} \frac{1}{N} \sum_{\mathbf{k}} \text{Tr}[G_{\mathbf{k}}(\omega + \Omega) \Lambda_{0,0}^{\text{para}}(\omega + \Omega; \Omega) G_{\mathbf{k}}(\omega + \Omega) \dot{\epsilon}_{\mathbf{k}} G_{\mathbf{k}}(\omega)]^< \\
& + \frac{i}{3} \int \frac{d\omega}{2\pi} \frac{1}{N} \sum_{\mathbf{k}} \text{Tr}[G_{\mathbf{k}}(\omega + \Omega) \Lambda_{1,0}^{\text{para}}(\omega; \Omega) G_{\mathbf{k}}(\omega) \dot{\epsilon}_{\mathbf{k}} G_{\mathbf{k}}(\omega)]^<, \tag{C13}
\end{aligned}$$

$$\begin{aligned}
\chi_{\text{H1}}^{(3)}(\Omega; \Omega, 0, 0) = & \frac{i}{6} \int \frac{d\omega}{2\pi} \frac{1}{N} \sum_{\mathbf{k}} \text{Tr}[\ddot{\epsilon}_{\mathbf{k}} \tau_3 G_{\mathbf{k}}(\omega) \ddot{\Delta}_{0,0}^{\text{dia}}(\Omega) \Lambda_{0,0}^{\tau_1}(\omega; \Omega) G_{\mathbf{k}}(\omega)]^< \\
& + \frac{i}{3} \int \frac{d\omega}{2\pi} \frac{1}{N} \sum_{\mathbf{k}} \text{Tr}[\ddot{\epsilon}_{\mathbf{k}} \tau_3 G_{\mathbf{k}}(\omega + \Omega) \ddot{\Delta}_{1,0}^{\text{dia}}(\Omega) \Lambda_{1,0}^{\tau_1}(\omega; \Omega) G_{\mathbf{k}}(\omega)]^<, \tag{C14}
\end{aligned}$$

$$\begin{aligned}
\chi_{\text{H2}}^{(3)}(\Omega; \Omega, 0, 0) = & \frac{i}{6} \int \frac{d\omega}{2\pi} \frac{1}{N} \sum_{\mathbf{k}} \text{Tr}[\ddot{\epsilon}_{\mathbf{k}} \tau_3 G_{\mathbf{k}}(\omega) \ddot{\Delta}_{0,0}^{\text{para}}(\Omega) \Lambda_{0,0}^{\tau_1}(\omega; \Omega) G_{\mathbf{k}}(\omega)]^< \\
& + \frac{i}{3} \int \frac{d\omega}{2\pi} \frac{1}{N} \sum_{\mathbf{k}} \text{Tr}[\ddot{\epsilon}_{\mathbf{k}} \tau_3 G_{\mathbf{k}}(\omega + \Omega) \ddot{\Delta}_{1,0}^{\text{para}}(\Omega) \Lambda_{1,0}^{\tau_1}(\omega; \Omega) G_{\mathbf{k}}(\omega)]^< \\
& + \frac{i}{6} \int \frac{d\omega}{2\pi} \frac{1}{N} \sum_{\mathbf{k}} \text{Tr}[\dot{\epsilon}_{\mathbf{k}} G_{\mathbf{k}}(\omega + \Omega) \dot{\epsilon}_{\mathbf{k}} G_{\mathbf{k}}(\omega) \ddot{\Delta}_{0,0}^{\text{dia}}(\Omega) \Lambda_{0,0}^{\tau_1}(\omega; \Omega) G_{\mathbf{k}}(\omega)]^< \\
& + \frac{i}{3} \int \frac{d\omega}{2\pi} \frac{1}{N} \sum_{\mathbf{k}} \text{Tr}[\dot{\epsilon}_{\mathbf{k}} G_{\mathbf{k}}(\omega + \Omega) \dot{\epsilon}_{\mathbf{k}} G_{\mathbf{k}}(\omega + \Omega) \ddot{\Delta}_{1,0}^{\text{dia}}(\Omega) \Lambda_{1,0}^{\tau_1}(\omega; \Omega) G_{\mathbf{k}}(\omega)]^< \\
& + \frac{i}{6} \int \frac{d\omega}{2\pi} \frac{1}{N} \sum_{\mathbf{k}} \text{Tr}[\dot{\epsilon}_{\mathbf{k}} G_{\mathbf{k}}(\omega + \Omega) \ddot{\Delta}_{0,0}^{\text{dia}}(\Omega) \Lambda_{0,0}^{\tau_1}(\omega + \Omega; \Omega) G_{\mathbf{k}}(\omega + \Omega) \dot{\epsilon}_{\mathbf{k}} G_{\mathbf{k}}(\omega)]^< \\
& + \frac{i}{3} \int \frac{d\omega}{2\pi} \frac{1}{N} \sum_{\mathbf{k}} \text{Tr}[\dot{\epsilon}_{\mathbf{k}} G_{\mathbf{k}}(\omega + \Omega) \ddot{\Delta}_{1,0}^{\text{dia}}(\Omega) \Lambda_{1,0}^{\tau_1}(\omega; \Omega) G_{\mathbf{k}}(\omega) \dot{\epsilon}_{\mathbf{k}} G_{\mathbf{k}}(\omega)]^<, \tag{C15}
\end{aligned}$$

$$\begin{aligned}
\chi_{\text{H3}}^{(3)}(\Omega; \Omega, 0, 0) = & \frac{i}{6} \int \frac{d\omega}{2\pi} \frac{1}{N} \sum_{\mathbf{k}} \text{Tr}[G_{\mathbf{k}}(\omega + \Omega) \dot{\epsilon}_{\mathbf{k}} G_{\mathbf{k}}(\omega) \ddot{\Delta}_{0,0}^{\text{para}}(\Omega) \Lambda_{0,0}^{\tau_1}(\omega; \Omega) G_{\mathbf{k}}(\omega)]^< \\
& + \frac{i}{3} \int \frac{d\omega}{2\pi} \frac{1}{N} \sum_{\mathbf{k}} \text{Tr}[G_{\mathbf{k}}(\omega + \Omega) \dot{\epsilon}_{\mathbf{k}} G_{\mathbf{k}}(\omega + \Omega) \ddot{\Delta}_{1,0}^{\text{para}}(\Omega) \Lambda_{1,0}^{\tau_1}(\omega; \Omega) G_{\mathbf{k}}(\omega)]^< \\
& + \frac{i}{6} \int \frac{d\omega}{2\pi} \frac{1}{N} \sum_{\mathbf{k}} \text{Tr}[G_{\mathbf{k}}(\omega + \Omega) \ddot{\Delta}_{0,0}^{\text{para}}(\Omega) \Lambda_{0,0}^{\tau_1}(\omega + \Omega; \Omega) G_{\mathbf{k}}(\omega + \Omega) \dot{\epsilon}_{\mathbf{k}} G_{\mathbf{k}}(\omega)]^< \\
& + \frac{i}{3} \int \frac{d\omega}{2\pi} \frac{1}{N} \sum_{\mathbf{k}} \text{Tr}[G_{\mathbf{k}}(\omega + \Omega) \ddot{\Delta}_{1,0}^{\text{para}}(\Omega) \Lambda_{1,0}^{\tau_1}(\omega; \Omega) G_{\mathbf{k}}(\omega) \dot{\epsilon}_{\mathbf{k}} G_{\mathbf{k}}(\omega)]^<. \tag{C16}
\end{aligned}$$

---

[1] S. Mukamel, *Principles of Nonlinear Optical Spectroscopy* (Oxford University Press, 1995).

[2] M. Cho, “Coherent two-dimensional optical spectroscopy,” *Chem. Rev.* **108**, 1331 (2008).

- [3] P. Hamm and M. Zanni, *Concepts and Methods of 2D Infrared Spectroscopy* (Cambridge University Press, Cambridge, 2011).
- [4] S. Biswas, J.-W. Kim, X. Zhang, and G. D. Scholes, “Coherent two-dimensional and broadband electronic spectroscopies,” *Chem. Rev.* **122**, 4257 (2022).
- [5] E. Fresch, F. V. A. Camargo, Q. Shen, C. C. Bellora, T. Pullerits, G. S. Engel, G. Cerullo, and E. Collini, “Two-dimensional electronic spectroscopy,” *Nat. Rev. Methods Primers* **3**, 84 (2023).
- [6] A. Liu, “Multidimensional terahertz probes of quantum materials,” *npj Quant. Mater.* **10**, 18 (2025).
- [7] C. Huang and M. Mootz and L. Luo and I. E. Perakis and J. Wang, “Unlocking Quantum Control and Multi-Order Correlations via Terahertz Two-Dimensional Coherent Spectroscopy,” arXiv:2507.02116.
- [8] N. Tsuji, I. Danshita, and S. Tsuchiya, “Higgs and Nambu-Goldstone modes in condensed matter physics,” in *Encyclopedia of Condensed Matter Physics (Second Edition)* (Academic Press, Oxford, 2024) 2nd ed., pp. 174–186.
- [9] P. W. Anderson, “Random-Phase Approximation in the Theory of Superconductivity,” *Phys. Rev.* **112**, 1900 (1958).
- [10] A. Schmid, “The approach to equilibrium in a pure superconductor the relaxation of the Cooper pair density,” *Phys. Kondens. Mater.* **8**, 129 (1968).
- [11] D. Pekker and C.M. Varma, “Amplitude/Higgs Modes in Condensed Matter Physics,” *Annu. Rev. Condens. Matter Phys.* **6**, 269 (2015).
- [12] R. Shimano and N. Tsuji, “Higgs Mode in Superconductors,” *Annu. Rev. Condens. Matter Phys.* **11**, 103 (2020).
- [13] A. Moor, A. F. Volkov, and K. B. Efetov, “Amplitude Higgs Mode and Admittance in Superconductors with a Moving Condensate,” *Phys. Rev. Lett.* **118**, 047001 (2017).
- [14] S. Nakamura, Y. Iida, Y. Murotani, R. Matsunaga, H. Terai, and R. Shimano, “Infrared Activation of the Higgs Mode by Supercurrent Injection in Superconducting NbN,” *Phys. Rev. Lett.* **122**, 257001 (2019).
- [15] T. Kubo, “Significant contributions of the Higgs mode and impurity-scattering self-energy corrections to the low-frequency complex conductivity in dc-biased superconducting devices,” *Phys. Rev. Appl.* **22**, 044042 (2024).
- [16] K. Wang, R. Boyack, and K. Levin, “Higgs amplitude mode in optical conductivity in the presence of a supercurrent: Gauge-invariant formulation with disorder,” *Phys. Rev. B* **111**, 144512 (2025).
- [17] R. Nagashima, T. Moulleron, and N. Tsuji, “Optically active Higgs and Leggett modes in multiband pair-density-wave superconductors with Lifshitz invariant,” *Phys. Rev. B* **112**, 024503 (2025).
- [18] G. Niederhoff, R. Kataoka, K. Takasan, and N. Tsuji, “Current-Enabled Optical Conductivity of Collective Modes in Unconventional Superconductors,” arXiv:2504.06642.
- [19] R. Sooryakumar and M. V. Klein, “Raman scattering by superconducting-gap excitations and their coupling to charge-density waves,” *Phys. Rev. Lett.* **45**, 660–662 (1980).
- [20] R. Sooryakumar and M. V. Klein, “Raman scattering from superconducting gap excitations in the presence of a magnetic field,” *Phys. Rev. B* **23**, 3213–3221 (1981).
- [21] P. B. Littlewood and C. M. Varma, “Gauge-Invariant Theory of the Dynamical Interaction of Charge Density Waves and Superconductivity,” *Phys. Rev. Lett.* **47**, 811–814 (1981).
- [22] P. B. Littlewood and C. M. Varma, “Amplitude collective modes in superconductors and their coupling to charge-density waves,” *Phys. Rev. B* **26**, 4883 (1982).
- [23] M.-A. Méasson, Y. Gallais, M. Cazayous, B. Clair, P. Rodière, L. Cario, and A. Sacuto, “Amplitude Higgs mode in the  $2H - \text{NbSe}_2$  superconductor,” *Phys. Rev. B* **89**, 060503 (2014).
- [24] R. Grasset, T. Cea, Y. Gallais, M. Cazayous, A. Sacuto, L. Cario, L. Benfatto, and M.-A. Méasson, “Higgs-mode radiance and charge-density-wave order in  $2H - \text{NbSe}_2$ ,” *Phys. Rev. B* **97**, 094502 (2018).
- [25] R. Grasset, Y. Gallais, A. Sacuto, M. Cazayous, S. Mañás Valero, E. Coronado, and M.-A. Méasson, “Pressure-Induced Collapse of the Charge Density Wave and Higgs Mode Visibility in  $2H - \text{TaS}_2$ ,” *Phys. Rev. Lett.* **122**, 127001 (2019).
- [26] R. Matsunaga, Y. I. Hamada, K. Makise, Y. Uzawa, H. Terai, Z. Wang, and R. Shimano, “Higgs Amplitude Mode in the BCS Superconductors  $\text{Nb}_{1-x}\text{Ti}_x\text{N}$  Induced by Terahertz Pulse Excitation,” *Phys. Rev. Lett.* **111**, 057002 (2013).
- [27] R. Matsunaga, N. Tsuji, H. Fujita, A. Sugioka, K. Makise, Y. Uzawa, H. Terai, Z. Wang, H. Aoki, and R. Shimano, “Light-induced collective pseudospin precession resonating with Higgs mode in a superconductor,” *Science* **345**, 1145 (2014).
- [28] K. Katsumi, N. Tsuji, Y. I. Hamada, R. Matsunaga, J. Schneeloch, R. D. Zhong, G. D. Gu, H. Aoki, Y. Gallais, and R. Shimano, “Higgs Mode in the  $d$ -Wave Superconductor  $\text{Bi}_2\text{Sr}_2\text{CaCu}_2\text{O}_{8+x}$  Driven by an Intense Terahertz Pulse,” *Phys. Rev. Lett.* **120**, 117001 (2018).
- [29] K. Katsumi, Z. Z. Li, H. Raffy, Y. Gallais, and R. Shimano, “Superconducting fluctuations probed by the Higgs mode in  $\text{Bi}_2\text{Sr}_2\text{CaCu}_2\text{O}_{8+x}$  thin films,” *Phys. Rev. B* **102**, 054510 (2020).
- [30] N. Tsuji and H. Aoki, “Theory of Anderson pseudospin resonance with Higgs mode in superconductors,” *Phys. Rev. B* **92**, 064508 (2015).
- [31] R. Matsunaga, N. Tsuji, K. Makise, H. Terai, H. Aoki, and R. Shimano, “Polarization-resolved terahertz third-harmonic generation in a single-crystal superconductor NbN: Dominance of the Higgs mode beyond the BCS approximation,” *Phys. Rev. B* **96**, 020505 (2017).
- [32] H. Chu, M.-J. Kim, K. Katsumi, S. Kovalev, R. D. Dawson, L. Schwarz, N. Yoshikawa, G. Kim, D. Putzky, Z. Z. Li, H. Raffy, S. Germanskiy, J.-C. Deinert, N. Awari, I. Ilyakov, B. Green, M. Chen, M. Bawatna, G. Cristiani, G. Logvenov, Y. Gallais, A. V. Boris, B. Keimer, A. P. Schnyder, D. Manske, M. Gensch, Z. Wang, R. Shimano, and S. Kaiser, “Phase-resolved Higgs response in superconducting cuprates,” *Nat. Commun.* **11**, 1793 (2020).
- [33] S. Kovalev, T. Dong, L.-Y. Shi, C. Reinhofer, T.-Q. Xu, H.-Z. Wang, Y. Wang, Z.-Z. Gan, S. German-skiy, J.-C. Deinert, I. Ilyakov, P. H. M. van Loosdrecht, D. Wu, N.-L. Wang, J. Demsar, and Z. Wang, “Band-selective third-harmonic generation in superconducting  $\text{MgB}_2$ : Possible evidence for the Higgs amplitude mode in the dirty limit,” *Phys. Rev. B* **104**, L140505 (2021).
- [34] K. Isoyama, N. Yoshikawa, K. Katsumi, J. Wong, N. Shikama, Y. Sakishita, F. Nabeshima, A. Maeda, and R. Shimano, “Light-induced enhancement of super-

- conductivity in iron-based superconductor  $\text{FeSe}_{0.5}\text{Te}_{0.5}$ ,” *Commun. Phys.* **4**, 160 (2021).
- [35] Z.-X. Wang, J.-R. Xue, H.-K. Shi, X.-Q. Jia, T. Lin, L.-Y. Shi, T. Dong, F. Wang, and N.-L. Wang, “Transient Higgs oscillations and high-order nonlinear light-Higgs coupling in a terahertz wave driven NbN superconductor,” *Phys. Rev. B* **105**, L100508 (2022).
- [36] K. Katsumi, M. Nishida, S. Kaiser, S. Miyasaka, S. Tajima, and R. Shimano, “Near-infrared light-induced superconducting-like state in underdoped  $\text{YBa}_2\text{Cu}_3\text{O}_y$  studied by *c*-axis terahertz third-harmonic generation,” *Phys. Rev. B* **107**, 214506 (2023).
- [37] M.-J. Kim, S. Kovalev, M. Udina, R. Haenel, G. Kim, M. Puviani, G. Cristiani, I. Ilyakov, T. V. A. G. de Oliveira, A. Ponomaryov, J.-C. Deinert, G. Logvenov, B. Keimer, D. Manske, L. Benfatto, and S. Kaiser, “Tracing the dynamics of superconducting order via transient terahertz third-harmonic generation,” *Sci. Adv.* **10**, eadi7598 (2024).
- [38] K. Katsumi, J. Fiore, M. Udina, R. Romero, D. Barbalas, J. Jesudasan, P. Raychaudhuri, G. Seibold, L. Benfatto, and N. P. Armitage, “Revealing Novel Aspects of Light-Matter Coupling by Terahertz Two-Dimensional Coherent Spectroscopy: The Case of the Amplitude Mode in Superconductors,” *Phys. Rev. Lett.* **132**, 256903 (2024).
- [39] K. Katsumi, J. Liang, R. Romero, K. Chen, X. Xi, and N. P. Armitage, “Amplitude Mode in a Multigap Superconductor  $\text{MgB}_2$  Investigated by Terahertz Two-Dimensional Coherent Spectroscopy,” *Phys. Rev. Lett.* **135**, 036902 (2025).
- [40] B. Cheng, D. Cheng, K. Lee, M. Mootz, C. Huang, L. Luo, Z. Chen, Y. Lee, B. Y. Wang, I. E. Perakis, Z.-X. Shen, H. Y. Hwang, and J. Wang, “Observation of cupratelike nonlinear terahertz responses in superconducting infinite-layer nickelates via two-dimensional coherent spectroscopy,” *Phys. Rev. B* **111**, 014519 (2025).
- [41] D. Chaudhuri and D. Barbalas and F. Mahmood and J. Liang and R. Romero III and A. Legros and X. He and H. Raffy and I. Bozovic and N. P. Armitage, “Planckian dissipation, anomalous high temperature THz non-linear response and energy relaxation in the strange metal state of the cuprate superconductors”, arXiv:2503.15646.
- [42] M. Mootz, L. Luo, C. Huang, J. Wang, and I. E. Perakis, “Multidimensional coherent spectroscopy of light-driven states and their collective modes in multiband superconductors,” *Phys. Rev. B* **109**, 014515 (2024).
- [43] A. Gómez Salvador, P. E. Dolgirev, M. H. Michael, A. Liu, D. Pavicevic, M. Fechner, A. Cavalleri, and E. Demler, “Principles of two-dimensional terahertz spectroscopy of collective excitations: The case of Josephson plasmons in layered superconductors,” *Phys. Rev. B* **110**, 094514 (2024).
- [44] J. Chen and P. Werner, “Multidimensional coherent spectroscopy of correlated lattice systems,” *npj Comput. Mater.* **11**, 127 (2025).
- [45] J. Chen and N. Tsuji and P. Werner, “Higgs mode in two-dimensional coherent spectroscopy of weak-coupling antiferromagnets”, arXiv:2504.21351.
- [46] D. C. Mattis and J. Bardeen, “Theory of the Anomalous Skin Effect in Normal and Superconducting Metals,” *Phys. Rev.* **111**, 412 (1958).
- [47] T. Jujo, “Quasiclassical Theory on Third-Harmonic Generation in Conventional Superconductors with Paramagnetic Impurities,” *J. Phys. Soc. Jpn.* **87**, 024704 (2018).
- [48] Y. Murotani and R. Shimano, “Nonlinear optical response of collective modes in multiband superconductors assisted by nonmagnetic impurities,” *Phys. Rev. B* **99**, 224510 (2019).
- [49] M. Silaev, “Nonlinear electromagnetic response and Higgs-mode excitation in BCS superconductors with impurities,” *Phys. Rev. B* **99**, 224511 (2019).
- [50] N. Tsuji and Y. Nomura, “Higgs-mode resonance in third harmonic generation in NbN superconductors: Multiband electron-phonon coupling, impurity scattering, and polarization-angle dependence,” *Phys. Rev. Res.* **2**, 043029 (2020).
- [51] G. Seibold, M. Udina, C. Castellani, and L. Benfatto, “Third harmonic generation from collective modes in disordered superconductors,” *Phys. Rev. B* **103**, 014512 (2021).
- [52] N. Tsuji, Y. Murakami, and H. Aoki, “Nonlinear light-Higgs coupling in superconductors beyond BCS: Effects of the retarded phonon-mediated interaction,” *Phys. Rev. B* **94**, 224519 (2016).
- [53] T. Cea, C. Castellani, and L. Benfatto, “Nonlinear optical effects and third-harmonic generation in superconductors: Cooper pairs versus Higgs mode contribution,” *Phys. Rev. B* **93**, 180507 (2016).
- [54] Typically, in lattice models one has  $v_F \sim Wa$ . In order to have a difference of several orders of magnitudes between  $\frac{v_F}{W}$  and  $L$ , we need at least  $L \gtrsim 10^2 a$ .
- [55] E. Abrahams, P. W. Anderson, D. C. Licciardello, and T. V. Ramakrishnan, “Scaling Theory of Localization: Absence of Quantum Diffusion in Two Dimensions,” *Phys. Rev. Lett.* **42**, 673 (1979).
- [56] P. A. Lee and D. S. Fisher, “Anderson Localization in Two Dimensions,” *Phys. Rev. Lett.* **47**, 882 (1981).
- [57] J. Rammer, *Quantum Field Theory of Non-equilibrium States* (Cambridge University Press, Cambridge, 2007).
- [58] A. A. Abrikosov and L. P. Gor’kov, “On the theory of superconducting alloys I. The electrodynamics of alloys at absolute zero”, *Sov. Phys. JETP* **8**, 1090 (1959).
- [59] L. V. Keldysh, “Diagrammatic technique for nonequilibrium processes”, *Sov. Phys. JETP* **20**, 1018 (1965).
- [60] H. Aoki, N. Tsuji, M. Eckstein, M. Kollar, T. Oka, and P. Werner, “Nonequilibrium dynamical mean-field theory and its applications,” *Rev. Mod. Phys.* **86**, 779 (2014).
- [61] T. Jujo, “Two-Photon Absorption by Impurity Scattering and Amplitude Mode in Conventional Superconductors,” *J. Phys. Soc. Jpn.* **84**, 114711 (2015).
- [62] B. L. Altshuler, D. Khmel’nitskii, A. I. Larkin, and P. A. Lee, “Magnetoresistance and Hall effect in a disordered two-dimensional electron gas,” *Phys. Rev. B* **22**, 5142–5153 (1980).
- [63] A. J. Leggett, “Number-Phase Fluctuations in Two-Band Superconductors,” *Prog. Theor. Phys.* **36**, 901 (1966).
- [64] H. Krull, D. Manske, G. S. Uhrig, and A. P. Schnyder, “Signatures of nonadiabatic BCS state dynamics in pump-probe conductivity,” *Phys. Rev. B* **90**, 014515 (2014).
- [65] Y. Murotani, N. Tsuji, and H. Aoki, “Theory of light-induced resonances with collective Higgs and Leggett modes in multiband superconductors,” *Phys. Rev. B* **95**, 104503 (2017).
- [66] T. Kamatani, S. Kitamura, N. Tsuji, R. Shimano, and T. Morimoto, “Optical response of the Leggett mode in multiband superconductors in the linear response regime,” *Phys. Rev. B* **105**, 094520 (2022).

- [67] R. Nagashima, S. Tian, R. Haenel, N. Tsuji, and D. Manske, “Classification of Lifshitz invariant in multi-band superconductors: An application to Leggett modes in the linear response regime in Kagome lattice models,” *Phys. Rev. Res.* **6**, 013120 (2024).
- [68] S. Klein and D. Manske, “Role of Higgs and Leggett modes for the third harmonic response in noncentrosymmetric superconductors,” *Phys. Rev. B* **110**, 014510 (2024).
- [69] B. A. Levitan, Y. Oreg, E. Berg, M. S. Rudner, and I. Iorsh, “Linear spectroscopy of collective modes and the gap structure in two-dimensional superconductors,” *Phys. Rev. Res.* **6**, 043170 (2024).
- [70] Y. Barlas and C. M. Varma, “Amplitude or Higgs modes in  $d$ -wave superconductors,” *Phys. Rev. B* **87**, 054503 (2013).
- [71] L. Schwarz, B. Fauseweh, N. Tsuji, N. Cheng, N. Bittner, H. Krull, M. Berciu, G. S. Uhrig, A. P. Schnyder, S. Kaiser, and D. Manske, “Classification and characterization of nonequilibrium Higgs modes in unconventional superconductors,” *Nat. Commun.* **11**, 287 (2020).
- [72] L. Schwarz and D. Manske, “Theory of driven Higgs oscillations and third-harmonic generation in unconventional superconductors,” *Phys. Rev. B* **101**, 184519 (2020).
- [73] C. Vaswani, J. H. Kang, M. Mootz, L. Luo, X. Yang, C. Sundahl, D. Cheng, C. Huang, R. H. J. Kim, Z. Liu, Y. G. Collantes, E. E. Hellstrom, I. E. Perakis, C. B. Eom, and J. Wang, “Light quantum control of persisting Higgs modes in iron-based superconductors,” *Nat. Commun.* **12**, 258 (2021).
- [74] N. R. Poniatowski, J. B. Curtis, A. Yacoby, and P. Narang, “Spectroscopic signatures of time-reversal symmetry breaking superconductivity,” *Commun. Phys.* **5**, 44 (2022).
- [75] A. Bardasis and J. R. Schrieffer, “Excitons and Plasmons in Superconductors,” *Phys. Rev.* **121**, 1050 (1961).
- [76] D. C. Langreth, in *Linear and Nonlinear Electron Transport in Solids*, edited by J. T. Devreese and V. E. van Doren (Plenum Press, New York, 1976).